Applied Thermal Engineering 230 (2023) 120848

Contents lists available at ScienceDirect

Applied Thermal Engineering

journal homepage: www.elsevier.com/locate/apthermeng

Research Paper

Convective heat transfer in a thermal chimney for freshwater production in geothermal total flow systems

Wenguang Li [a], Guopeng Yu [b], Zhibin Yu [a,*]

[a] School of Engineering, University of Glasgow, Glasgow G12 8QQ, UK
[b] Sino-French Institute of Nuclear Engineering and Technology, Sun Yat-Sen University, Zhuhai 519082, China

ARTICLE INFO

Keywords:
Thermal performance
Thermal chimney
Nusselt number
Geothermal energy
Convective heat transfer
Computational fluid dynamics

ABSTRACT

The convective heat transfer of air in a laboratory-scale thermal chimney with rectangular cross-section of constant area and two row electrical heaters simulating two heat exchangers was studied experimentally and numerically at 60–200 ℃ nominal temperatures of the top row heaters, 100 ℃ of the low row heaters and 20 ℃ ambient temperature to verify our design concept on freshwater production in geothermal total flow systems. Computational fluid dynamics simulations of air convective heat transfer were performed in ANSYS 2019R CFX based on the three-dimensional, steady Reynolds-averaged Navier-Stokes equations, Boussinesq buoyancy model, $k-\omega$ turbulence model, and energy equation. The thermal radiation between heater surfaces and chimney walls was considered. The overall thermal and heat transfer characteristics, temperature and flow fields in the chimney were obtained. Effects of boundary condition of heater surface and thermal radiation between two row heaters on heat transfer were discussed. The thermal characteristics of the chimney with two row heaters are better than that with single row heaters. The predicted thermal power and convective Nusselt number agree with the experimental data, and the convective Nusselt number of the low row heaters is enhanced by (11.6–29.8) % compared with the single row heaters. The optimal operating nominal temperature of top row heaters should be higher than 140 ℃, and the optimal centre-to-centre row gap ratio is 5. Multiple jets in the gaps among the heaters and temperature jump crossing each row were observed. The maximum velocity and temperature jump rise with increasing heater nominal temperature.

1. Introduction

Geothermal energy is a sort of renewable energy that is available year-long. Geothermal energy can be utilised directly for heating or transformed to electricity with turbines and generators, depending on geothermal water and/or steam temperature. Direct steam system, single-flash or dual-flash system, total flow system and binary system are commonly applied to generate electricity with geothermal energy [1,2]. In the direct steam and single-flash or dual-flash system, the steam experiences a typical Rankine cycle. The total flow system involves a trilateral flash cycle [3–8]. In the binary system, however, except the Rankine cycle or trilateral flash cycle of water and steam, there is an additional organic Rankine cycle [9–11] or carbon dioxide (CO2) Brayton cycle [12] or Kalina cycle of the mixture of water and ammonia [13–15]. The additional cycle is driven by the fluid discharged from the flashing vessel [9,10,12–14] or from the turbine [15].

In parallel, it is shown that geothermal heat can play a new role in the global water crisis and climate protection after the geothermal heat finds applications in water desalination and treatment sectors [16] and produces water and power simultaneously in Australia, Caribbean Islands, Central America, India, Israel, Saudi Arabia, UAE, USA, and Sub-Saharan Africa [17]. Further, combined geothermal electricity generation and seawater desalination systems were proposed and summarised [18]. Particularly, integrated organic Rankine cycle driven by geothermal heat with seawater multi-effect distillation desalination systems were developed and assessed [19–23]. A novel brackish water greenhouse desalination unit was proposed in [24] to harvest freshwater from abundant sea/brackish water resources using geothermal energy in Algeria. Using geothermal energy to power brackish water greenhouse desalination units has a notable advantage, which geothermal energy can supply power without any intermittence, over other renewable resources such as solar or wind energy. Two cases of geothermal brine reuse for both energy and freshwater production were assessed based on process, design and technical–economic analyses and an approach for evaluating the exergy efficiency of the processes was present [25].

* Corresponding author at: School of Engineering, University of Glasgow, Glasgow G12 8QQ, UK.
E-mail addresses: Wenguang.Li@glasgow.ac.uk (W. Li), yugp3@mail.sysu.edu.cn (G. Yu), Zhibin.Yu@glasgow.ac.uk (Z. Yu).

https://doi.org/10.1016/j.applthermaleng.2023.120848
Received 13 January 2023; Received in revised form 16 April 2023; Accepted 21 May 2023
Available online 24 May 2023
1359-4311/© 2023 The Author(s). Published by Elsevier Ltd. This is an open access article under the CC BY license (http://creativecommons.org/licenses/by/4.0/).

Nomenclature

a	width of inner cross-section of the chimney, a=280 mm
A	area of the surface of a heater exposed to the inner air body, $A=\pi dl$, m^2
b	depth of inner cross-section of the chimney, b=190 mm
c_p	specific heat capacity of air at constant pressure, J/kg K
C_3	turbulence dissipation coefficient, $C_3 = 1$ for the Boussinesq buoyancy model
d	heater diameter, d=16 mm
d_h	hydraulic diameter of the chimney, defined in Eq. (10)
g_i	gravity acceleration component in i coordinate direction, $g_1=g_3 = 0$, g_2=9.81 m/s^2
h	static enthalpy of air, m^2/s^2
h_{tot}	total enthalpy of air, $h_{tot} = h + u_iu_i/2 + k$, m^2/s^2
$I(\boldsymbol{r},\boldsymbol{s})$	thermal radiation intensity at wall, W/m^2
I_b	black body thermal radiation intensity, W/m^2
$I_b(T_w)$	blackbody thermal radiation intensity emitted from a solid surface at T_w, W/m^2
k	turbulent kinetic energy of air, $k = \overline{u_i'^2}/2$, m^2/s^2
l	heater length exposed to the air in the chimney, l=190 mm
m_f	air mass flow rate through the chimney, kg/s
m_{f0}	air mass flow rate through the chimney with single row of heaters, kg/s
$\boldsymbol{n}$	outwards normal vector of wall
N	number of heaters in the top or low row, N=10
Nu_c	convective Nusselt number
Nu_r	radiative equivalent Nusselt number
Nu_t	total Nusselt number
p	static pressure of air, Pa
P_k	turbulence production term in the k equation of Eq. (4), W/m^3
P_{kb}	buoyancy production term the in the k equation of Eq. (4), W/m^3
P_{low}	thermal power of a heater in the low row, W
Pr	Prandtl number of air,Pr $= \mu c_p/\lambda$
Pr_t	turbulent Prandtl number, Pr_t=0.85
$P_{\omega b}$	buoyancy production term in the ω equation of Eq. (4), kg/m^3 s^2
q_c	wall convective heat flux, W/m^2
q_{low}	given wall heat flux across the surface of a heater in the low row, W/m^2
q_r	wall radiative heat flux, W/m^2
q_t	total wall heat flux, W/m^2
q_{top}	given wall heat flux through the surface of a heater in the top row, W/m^2
q_w	heat flux through the wall, defined in Eq. (6), W/m^2
Q_L	energy loss through the ground floor and chimney walls, W
Q_r	mean thermal radiation power, W
$Q_{r,j}$	thermal radiation power from the heater j in the top row to the heater i in the low row expressed by Eq. (13), W
$\boldsymbol{r}$	radius vector of a point on solid surface
Re	Reynolds number of the chimney, defined in Eq. (10)
Re_d	Reynolds number around the heaters, defined in Eq. (10)
$\boldsymbol{s}$	thermal radiation direction at wall
s_i	source term in the momentum equation in i coordinate direction, W/m^3
$\boldsymbol{s}'$	dummy variable in the integral of Eq. (7)
T	air local temperature, K
T_f	bulk temperature of the air in the chimney, $T_f = 0.5(T_{f1} + T_{f2})$, K
T_{f1}, T_{f2}	air temperatures at the chimney inlet and outlet, K
T_{low}	nominal temperature of the low row heaters, K
T_{ref}	reference ambient temperature, T_{ref}=20 °C
T_{top}	nominal temperature of the top row heaters, K
T_w	temperature at wall, K
T^+	dimensionless temperature
u_f	air characteristic or bulk velocity, m/s
u_{f1}, u_{f2}	air velocity at the inlet and outlet of the chimney, m/s
u_i, u_j	Reynolds-averaged air velocity components in i, j coordinate directions, respectively, m/s
u_τ	friction velocity at wall, m/s
u_i'	fluctuating air velocity component in i coordinate direction, m/s
y_n	distance between the first and second grid points off wall, m
y^+	dimensionless distance from wall,$y^+ = u_\tau y_n/\nu$

Greek

β	thermal expansivity of air, 1/K
β_k, $\beta_{\omega1}$, $\beta_{\omega2}$	model constants in Eq. (4), $\beta_k = 0.09$, $\beta_{\omega1} = 5/9$, $\beta_{\omega2} = 0.075$
Γ	auxiliary variable in Eq. (6)
δ_{ij}	Kronecker delta, δ_{ij}=0 if $i \neq j$ or$\delta_{ij} = 1$
Δ_{ij}	centre-to-centre gap between heater i in the low row and heater j in the top row, mm
ΔT_f	temperature rise of air across the chimney, K
Δx	centre-to-centre gap between two heaters in a row, mm
Δy	centre-to-centre gap between two rows of heaters, mm
ε	emissivity of heater surface or chimney inside walls or ground floor
η_{th}	energy gain coefficient of the chimney, defined by Eq. (9)
λ	thermal conductivity of air, W/m K
μ	dynamic viscosity of air, Pa.s
μ_t	turbulent eddy viscosity, $\mu_t = \rho k/\omega$, Pa. s
ν	kinematic viscosity of air, m^2/s
ρ	density of air, kg/m^3
ρ_{ref}	density of air at T_{ref}, kg/m^3
$-\rho\overline{u_j'h}$	Reynolds flux, W/m^2
$-\rho\overline{u_i'u_j'}$	Reynolds stresses of air flow, Pa
σ	Stefan-Boltzmann constant, σ=5.67037442 × 10^{-8} W/m^2 K^4
σ_b	turbulent Schmidt number,$\sigma_b = 0.9$
σ_k, σ_ω	model constants in Eq. (4), $\sigma_k = \sigma_\omega = 2$
τ_{ij}	shear stress tensor of air flow, Pa
ω	turbulent kinetic energy dissipation frequency, 1/s
Ω	solid angle, rad
Ω'	dummy variable of solid angle Ω

Subscripts

i, j	coordinate index of Cartesian coordinate system, i, j=1, 2, 3
i, j	index of the heaters in the low and top rows in Fig. 3, Eqs. (13) and (14)

Abbreviations

2D	two-dimensional
3D	three-dimensional
CFD	computational fluid dynamics
CO2	carbon dioxide
PID	proportional integral derivative
PIV	particle image velocimetry
RANS	Reynolds-averaged Navier-Stokes
RTD	resistance temperature detector

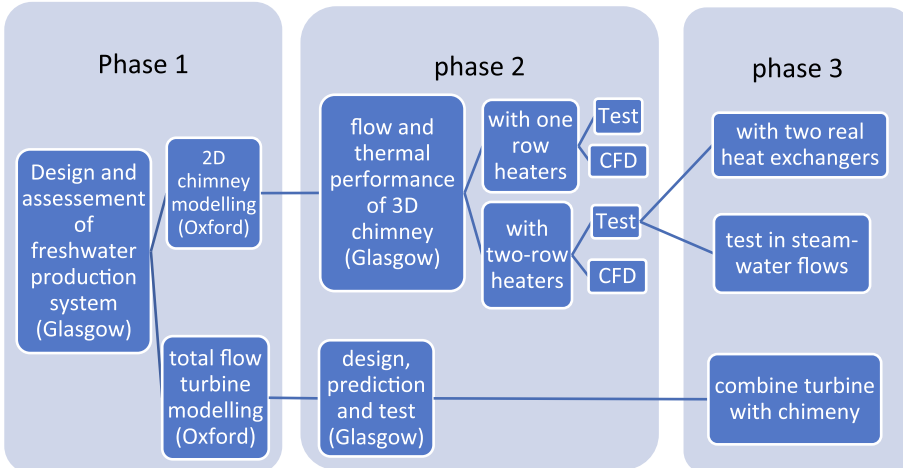

Fig. 1. Flowchart of the freshwater production project based on geothermal energy sources.

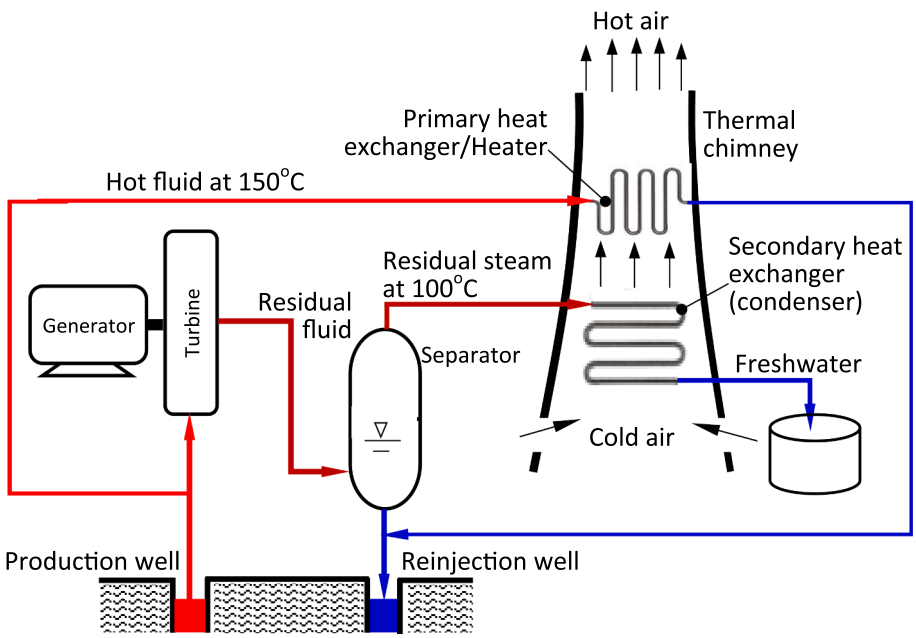

Fig. 2. Total flow system with thermal chimney to produce electricity and freshwater simultaneously from the residual fluid discharged by a two-phase flow turbine which extracts electric power from a hot fluid in a geothermal source at around 150 °C.

Traditional desalination technology and renewable energy-integrated desalination processes, especially geothermal-based seawater desalination, were reviewed in [26] and it is suggested that the use of geothermal energy as a new renewable energy source should be put on the table in the future.

To mitigate freshwater storage, energy crisis and farmland degradation in northern Victoria, Australia, saline water was heated to around 80 ℃ in a solar pond, then went into a disc turbine, and was vapourised in it. The turbine was driven by the steam to generate electricity with a generator, the steam was condensed in a container by using a heat exchanger of cold water. This is the first proposal for freshwater and power co-generation systems [27,28]. This system was improved by putting the turbine and the heat exchanger into a continuous large pipe with 105° bend [29]. A freshwater and power co-generation system using 60–70 ℃ brine from geothermal sources in Victoria, Australia was developed, and the solar pond was removed and the 105° bend was replaced with a 180° bend [30,31].

To face both challenges in shortage of electricity and water scarcity in eastern Africa, the feasibility of using a geothermal water source to produce both freshwater and electricity was explored in a project in our research group. The flowchart of the project is illustrated in Fig. 1. In phase 1, a freshwater production system from the brine discharged by the turbine in a geothermal total flow system was proposed [32]. It was shown that the freshwater output could be 2.7 times higher than the direct steam and single-flash systems [33] and more than 1/3 of total wellhead discharge could be recovered [34] for liquid-dominated geothermal sources. The total flow turbine modelling was referred to [35] and [36] and ignored here.

In that system shown in Fig. 2, as a novel design concept a thermal chimney with two heat exchangers, one is primary heat exchanger, and one is secondary heat exchanger (condenser), was proposed and employed to produce freshwater from the brine discharged by the total flow turbine. A stream of hot fluid from the wellhead flows through the primary exchanger. The residual steam discharged by the turbine enters the secondary heat exchanger to be condensed. The fluid bulk temperature in the primary heat exchanger is higher than the secondary heat exchanger, and the temperature of the two heat exchangers is higher than the air in the chimney. Hence, the air is heated and becomes warm

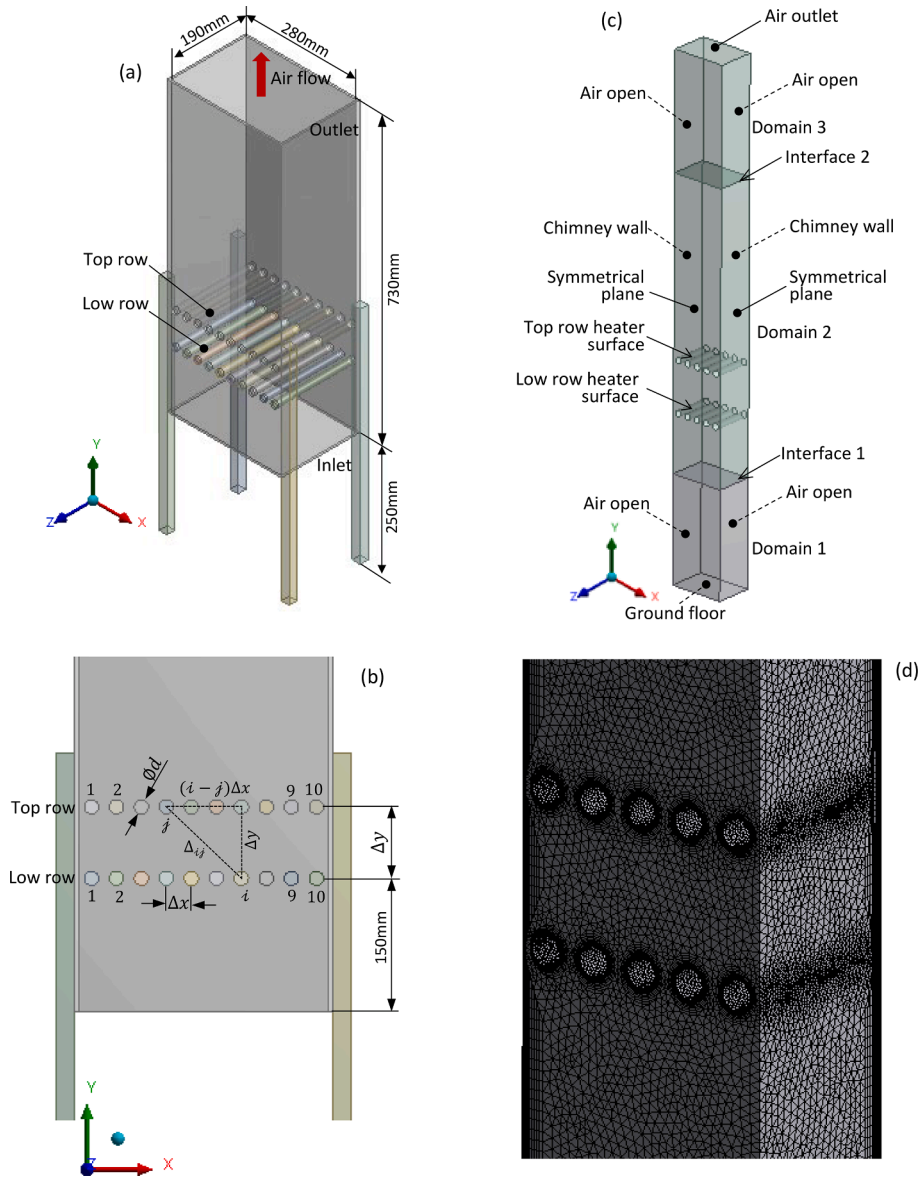

Fig. 3. Configuration, dimension, fluid domain and mesh closed-up of the experimental chimney, (a) 3D shape of the chimney, (b) definition of gap between two row heaters and gap between two heaters, (c) fluid domain, (d) mesh closed-up.

and flows upwards in the chimney owing to buoyancy effect. The cold air enters the chimney from the holes near the chimney's bottom to fill the space left by the warm air. The cold air generates a cooling effect on the secondary heat exchanger. If the effect is strong enough, the temperature of the residual steam goes down and the steam condenses to produce freshwater. The primary heat exchanger intensifies the air draft flow in the chimney and increases Reynolds number around the secondary heat exchanger to enhance convective heat transfer between the air and the exchanger. Therefore, the primary heat exchanger can reduce the size of the chimney and the secondary heat exchanger.

Compared with the freshwater and power co-generation systems in [27–30], the novelty of our proposal is that a thermal chimney is used as an air cooling device and an additional heat exchanger is installed in the chimney to enhance convective heat transfer over the condenser. Since the chimney is simple in construction, it is easily built and maintained, and applicable to large-scale geothermal power plants. The complicated and costed water-cooling system is not needed.

In Phase 1, two-dimensional (2D) unsteady and steady natural convection of air in a channel around a row of isothermal horizontal cylinders was modelled with computational fluid dynamics (CFD) software-ANSYS Fluent by using the Boussinesq buoyancy assumption and the effect of centre-to-centre cylinder gap ratio on Nusselt number was investigated [37]. 2D unsteady and steady natural convective heat transfer of air in a channel with two rows of isothermal horizontal cylinders was simulated by using ANSYS Fluent in the Boussinesq buoyancy condition based on the Reynolds-averaged Navier-Stokes (RANS) equations, shear stress transport turbulence model and energy equation [38]. It was shown that there was a best centre-to-centre ratio to the natural draft velocity and the centre-to-centre row gap ratio influenced flow patterns in the chimney.

In Phase 2, a three-dimensional (3D) thermal chimney in constant rectangular cross-section area with a primary heat exchanger was designed. The primary heat exchanger was replaced with a row of 10 electrical heaters distributed horizontally and evenly in the chimney. The temperature longitudinal profiles on the heaters were measured by using forward-looking infrared camera. The measured temperature profile was modelled and included in ANSYS CFX simulations as temperature boundary conditions and the radiation from the heaters to the air was taken into account. Velocity fields predicted by CFD were validated with air velocities measured by employing particle image

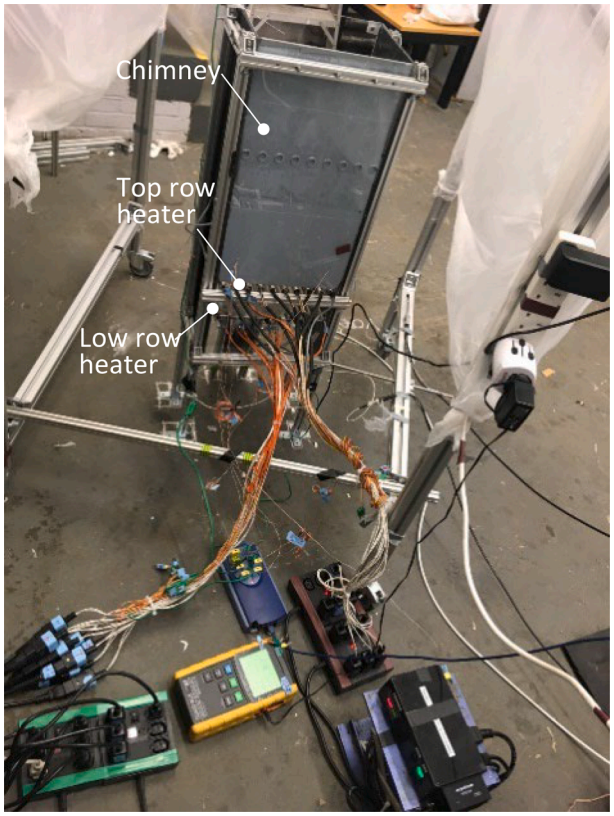

Fig. 4. Experimental set-up of the thermal chimney.

Table 1
Information on instrument and errors in measurement.

Instrument	Brand and type	Error
PID controller	OMEGA™	±0.5℃
Wattmeter	Voltech power analyser PM 1000+	0.1% (reading) + 0.1% (range)
Thermal couples of heaters	OMEGA Self-Adhesive Thermocouples	±0.2%
Thermal couples of airflow	OMEGA RTD probe	±0.2%

Table 2
Physical property constants of air, acrylic sheet and stainless steel and cement ground floor at 20 °C.

Constant	Air	Acrylic sheet with full black painting	Stainless steel with partial black painting	Cement ground floor
Density ρ(kg/m^3)	1.1888	N/A		
Specific heat capacity c_p (J/kg K)	1006.1			
Thermal conductivity λ (W/m.K)	2.5873 × 10^{-2}			
Thermal expansivity β (1/K)	3.4112 × 10^{-3}			
Dynamic viscosity μ (Pa. s)	1.8205 × 10^{-5}			
Kinematic viscosity ν (m^2/s)	1.5314 × 10^{-5}			
Emissivity ε	N/A	0.94	0.27	0.95

Table 3
Element size, mesh quality, inflation mesh and energy gain coefficient of the chimney.

Mesh name			Mesh 1	Mesh 2	Mesh 3
Element size (mm)			5	3.75	2.5
Number of nodes			325,876	508,664	1,192,102
Number of elements	Hex8		60,648 (8%)	140,600 (12.3%)	485,184 (19.2%)
	Tet4		322,351 (42.3%)	495,825 (43.4%)	1,141,883 (45.1%)
	Wed6		373,042 (49%)	499,177 (43.8%)	896,431 (35.4%)
	Pry5		5,183 (0.7%)	5,316 (0.5%)	6,088 (0.3%)
	Total		761,224	1,140,918	2,529,586
Mesh quality	Element quality		0.5719 ± 0.3039	0.6307 ± 0.2983	0.7271 ± 0.2665
	Aspect ratio		4.9109 ± 4.7580	4.0968 ± 3.8798	2.9415 ± 2.6206
	Skewness		0.2251 ± 0.1671	0.2066 ± 0.1618	0.1832 ± 0.1572
	Orthogonal quality		0.7741 ± 0.1665	0.7927 ± 0.1613	0.7927 ± 0.1613
Inflation mesh for boundary layer	First layer height (mm)	Heater	0.25	0.25	0.25
		Chimney wall	0.25	0.25	0.25
	Number of layers	Heater	15	15	15
		Chimney wall	13	13	13
	Growth rate	Heater	1.2	1.2	1.2
		Chimney wall	1.2	1.2	1.2
	y^+	Top row	0.9860	0.9243	0.9577
		Low row	1.1304	1.1745	1.1151
Energy gain coefficient, η_{th}			0.8026	0.7788	0.7806

Hex8-eight-node hexahedral element, Tet4-four-node tetrahedral element, Wed6-six-node wedge element, Pry5-five-node pyramidal element, $y^+ = u_\tau y_n/\nu$, u_τ-friction velocity at wall, y_n-distance between the first and second grid points off the wall.

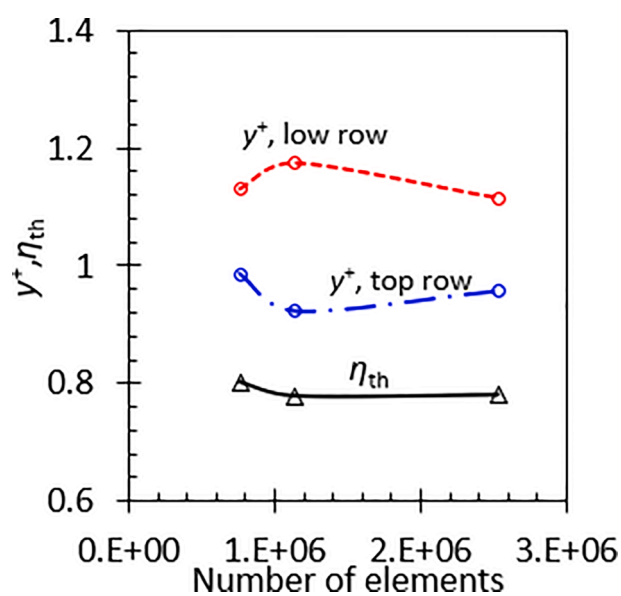

Fig. 5. y^+ of the heaters in the top and low rows and thermal coefficient of the chimney η_{th} are plotted as a function of number of elements of Mesh 1, 2 and 3.

velocimetry (PIV) in the chimney [39]. Further, the air flow fields in the mid-span in the chimneys were mapped by using PIV when the two heat exchangers were replaced with two rows of electrical heaters distributed horizontally and evenly in the chimney [40]. Unfortunately, the convective heat transfer in the 3D chimney with primary and secondary heat exchangers has not been investigated so far. The effect of the gap

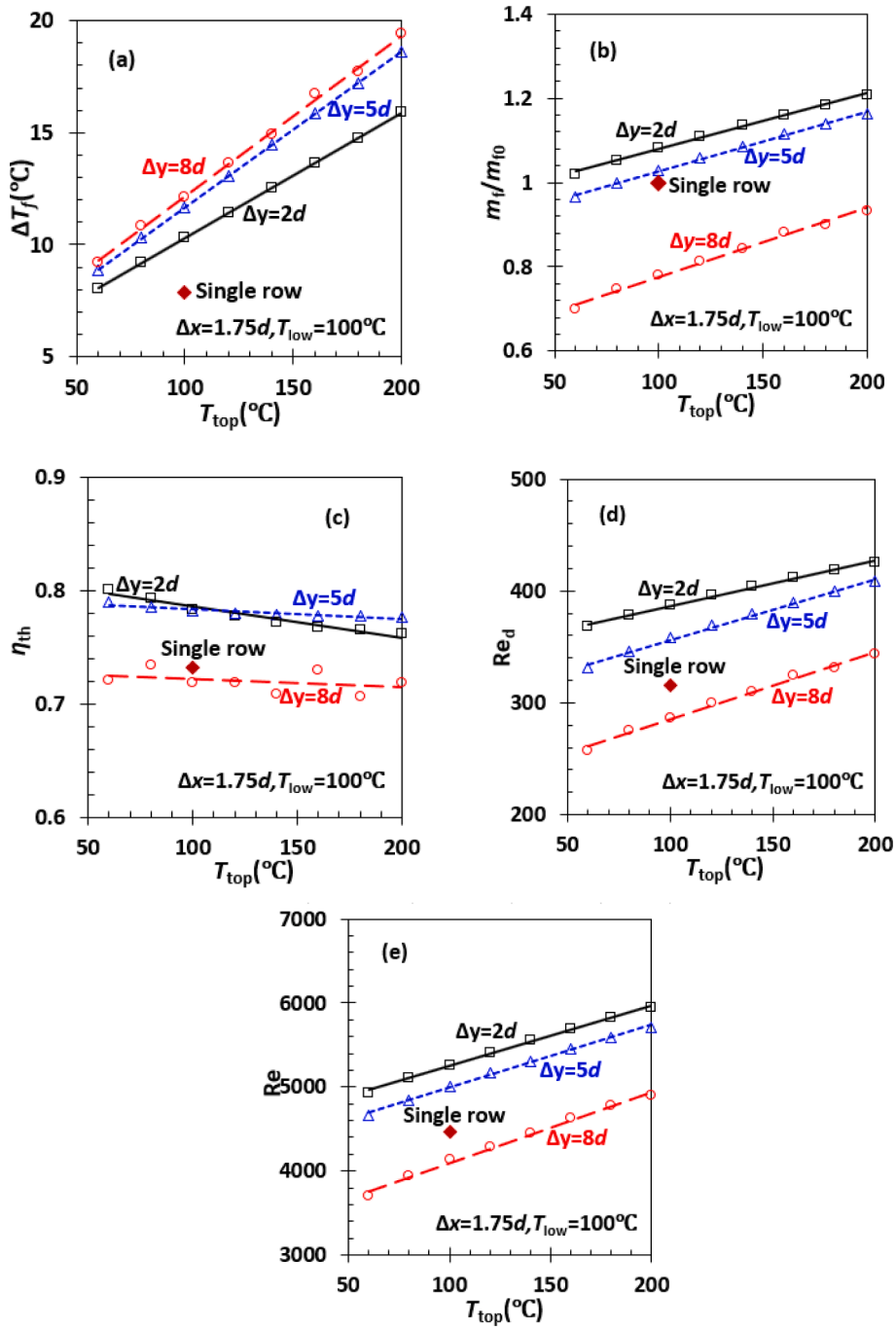

Fig. 6. Overall thermal performance of the thermal chimney in terms of temperature of the top row heaters at Δy = 2d, 5d, and 8d but fixed Δx = 1.75d and T_{low} = 100 ℃, (a) temperature rise ΔT_f, (b) dimensionless mass flow of air m_f/m_{f0}, (c) energy gain coefficient η_{th}, (d) Reynolds number around heaters Re_d, (e) Reynolds number of the chimney Re, the data of the chimney with single row heaters are from [39].

between two heat exchangers on the heat transfer in the chimney is unknown. These two matters of fact will hamper the design and optimisation of the chimney.

In this paper, the 3D thermal chimney for PIV test in [40] was employed as a physical model, and the primary heat exchanger and secondary heat exchanger in the chimney were replaced with two rows of electrical heating cylinders to mimic coil tube heat exchangers. The air in the chimney was heated with the two row heaters to investigate heating effect of the primary heat exchanger on the air and cooling effect of the air on the secondary heat exchanger. In experiment, the temperature of the top row heaters varied from 60 °C to 200 °C, while the temperature of the low row heaters remained at 100 °C. The flow and temperature of the air were measured at the inlet and outlet of the chimney. The centre-to-centre row gap ratios were specified as 2, 5 and 8 but the centre-to-centre cylinder gap ratio in two rows was fixed at 1.75. Meanwhile, the natural convective heat transfer and fluid flow in the chimney were simulated in ANSYS 2019R2 CFX based on the RANS equations, k-ω turbulence model and energy equation in terms of the Boussinesq buoyancy assumption. The radiation effect of surface-to-surface was considered by using discrete transfer method. The optimal centre-to-centre row gap ratio was determined. The outcomes will be significant to the design of thermal chimneys for geothermal freshwater and power cogeneration systems.

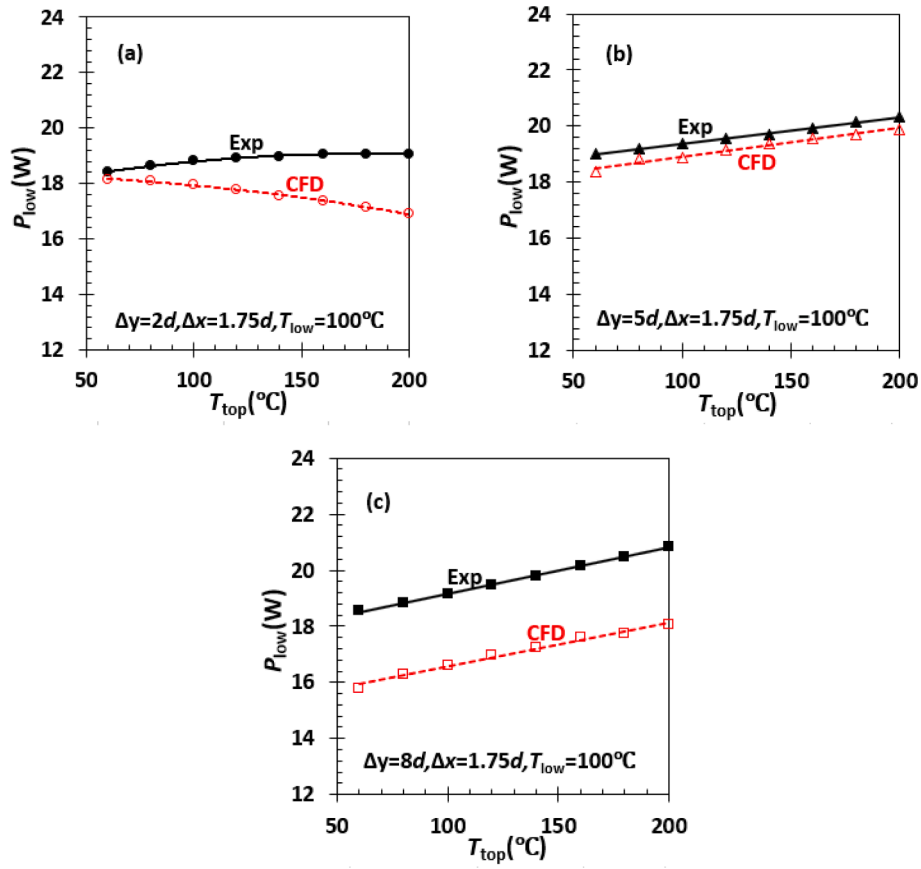

Fig. 7. Experimental electrical power of one heater in the low row is compared with the thermal power calculated in CFD simulations atΔy = 2d, 5d, 8d and fixedΔx = 1.75d, T_{low}=100 ℃, Exp-experimental data.

2. Chimney, test rig and CFD models

2.1. Chimney and test rig

The experimental thermal chimney with constant rectangular cross-sectional area was designed, fabricated, and illustrated with major dimensions in Fig. 3. The chimney is made of four 5 mm thick transparent acrylic sheets and supported on four aluminium legs. There are two rows of holes distributed horizontally and uniformly through a pair of sheets to accommodate 10 electrical cylindrical cartridge heaters with 16 mm dimeter (d) and 200 mm length. The top row heaters serve as the primary heat exchanger, while the low row heaters are used as the secondary heat exchanger. The centre-to-centre heater gap between two heaters Δx, see Fig. 3, is specified to be the optimal value of 1.75d, which was determined based on 2D CFD simulations of natural convective heat transfer over one row of isothermal cylinders in a 2D chimney conducted in [37], and the corresponding centre-to-centre heater gap ratio $\Delta x/d$ is equal to 1.75. The centre-to-centre row gap Δy, shown in Fig. 3, is selected to be 2d, 5d and 8d, resulting the centre-to-centre row gap ratios$\Delta y/d$ = 2, 5, 8 to clarify the effect of the gap on convective heat transfer over the heat exchangers.

The experimental set-up or rig of the thermal chimney is illustrated in Fig. 4 and the corresponding information about the instrument used in the rig is listed in Table 1. The thermocouples were glued on the surface of one cartridge heater each in the top and low row. Two sets of OMEGA^{TM} PID (proportional integral derivative) controller with solid state relays were connected to the power supply of the lower and top row heaters and the thermocouples to control the heater surface temperature. One set of PID controls the low row heaters temperature at 100 °C to mimic the outside surface of steam condensation tubes. The other set of PID controls the top row heater's temperature at 60, 80, 100, 120, 140, 160, 180, 200 ℃, respectively. The electrical power consumed by the heater in the low row was measured by using a digital Wattmeter instantly. The air temperature and ambient temperature were monitored as well. The experimental data were taken and saved on the hard drive after the heat balance state, i.e., steady state, was achieved. The experimental procedure is described as follows:

(1) Charge the lower row heaters to 100 ℃ till steady state;
(2) Charge the top row heaters to set an expected temperature till steady state;
(3) Record power and temperature of the lower row heaters;
(4) Record the temperature of in-/out- airflow, and the ambient temperature.

2.2. Computational models

Radiative heat transfer was not taken into account in 2D natural heat transfer over isothermal cylinder rows in a 2D chimney in [37,38]. Although radiation from the cylindrical heaters to the air in a 3D chimney was included in the natural heat transfer in the 3D chimney [39], the surface-to-surface radiation between the two heater rows and the radiation between the heaters and the four chimney walls have been ignored. These surface-to-surface radiations may be important at a small row gap ratio $\Delta y/d$ when the top row heaters are at a high temperature.

To take the surface-to-surface radiation into account, only three fluid domains are created as shown in Fig. 3, the first one is the air between the chimney inlet and the ground floor, the second one is the air inside the chimney and the last one is the air body covering 300 mm downstream the chimney. Since numerical computations of surface-to-surface radiation require fine mesh, it is assumed that the airflow is symmetrical about two geometrically symmetrical planes of the chimney, and only ¼

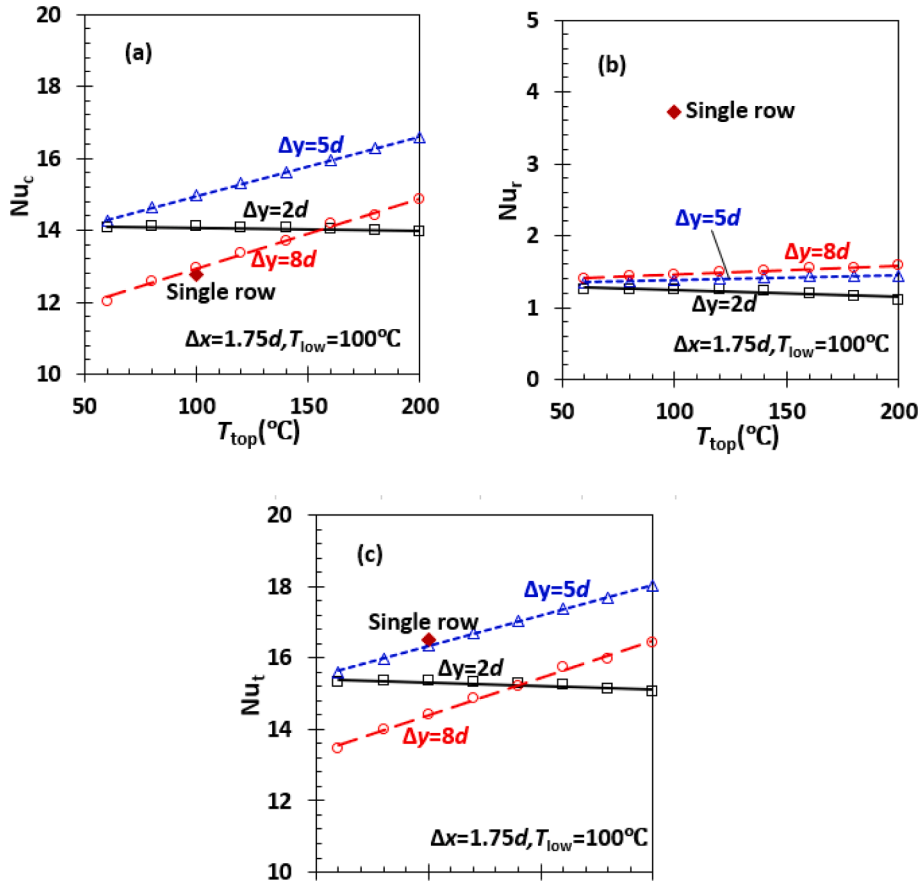

Fig. 8. Convective Nusselt number Nu_c, radiative Nusselt number Nu_r and total Nusselt number Nu_t predicted in CFD simulations against the temperature of the top row heaters at$\Delta x = 1.75d$ and $T_{low} = 100$ ℃, (a) Nu_c, (b) Nu_r, and (c) Nu_t, the data of the single row heaters are from [39].

fluid domain was involved in CFD simulations. Further, the heat conduction in the chimney walls is omitted but the walls are assigned with ambient temperature and a certain emissivity to implement surface-to-surface radiation computation. Like [39] the solid bodies of the electrical heaters are removed from the geometrical model; instead, their surfaces contacting with the inner air body, as shown in Fig. 3, become walls, and the surfaces can be subject to a known wall heat flux.

The CFD software-ANSYS 2019R2 CFX was adopted to simulate the natural convective heat transfer in the experimental thermal chimney and predict its thermal performance. The governing equations of the airflow inside the chimney include 3D steady RANS equations and thermal energy equation as follows [41]:

$$\begin{cases} \frac{\partial}{\partial x_j}(\rho u_j) = 0 \\ \frac{\partial}{\partial x_j}(\rho u_i u_j) = -\frac{\partial p}{\partial x_i} + \frac{\partial}{x_j}\left(\tau_{ij} - \rho\overline{u_i' u_j'}\right) + s_i \\ \frac{\partial}{\partial x_j}(\rho u_j h_{tot}) = \frac{\partial}{\partial x_j}\left(\lambda\frac{\partial T}{\partial x_j} - \rho\overline{u_j' h}\right) + \frac{\partial}{\partial x_j}\left[u_i\left(\tau_{ij} - \rho\overline{u_i' u_j'}\right)\right] \end{cases} \quad (1)$$

where ρ is density of air, u_i is an averaged velocity component of air, p is static pressure of air, τ_{ij} is shear stress tensor of airflow, i and j are coordinate index of Cartesian coordinate system, i, j=1,2,3, s_i is a source term in the momentum equations, λ is thermal conductivity of air, h_{tot} is total enthalpy of air, $h_{tot} = h + u_i u_i/2 + k$, h is static enthalpy of air,k is turbulent kinetic energy, $k = \overline{u_i'^2}/2$, u_i' is a fluctuating velocity component. The term $\partial\left[u_i\left(\tau_{ij} - \rho\overline{u_i' u_j'}\right)\right]/\partial x_j$ in the thermal energy equation represents the viscous dissipation, and can be neglected due to the low air velocity in the chimney.

The natural convective heat transfer of air in the thermal chimney is driven by the buoyance effect. The Bousssinsq model is valid for this kind of heat transfer as long as the air temperature difference across a domain is smaller than 28.6 °C at 15 °C ambient temperature and 1 atm atmosphere pressure [42]. Because the air temperature rise (<20 °C) is low across the chimney, the source term in the momentum equations in Eq. (1) should conform to the Boussinesq model, and is written as [41]:

$$s_i = -\rho_{ref}\beta(T - T_{ref})g_i \quad (2)$$

where T_{ref} is the reference ambient temperature, T_{ref}=20 °C, ρ_{ref} is the air density at T_{ref}, β is the thermal expansivity of air, g_i is the gravity acceleration component in i coordinate direction, g_1=g_3 = 0, g_2=9.81 m/s^2 here, ρ_{ref}, β and λ values are listed in Table 2.

The term $-\rho\overline{u_i' u_j'}$ in Eq. (1) are the Reynolds stresses caused by turbulent velocity fluctuation and need to be modelled. The airflow in the fluid domains shown in Fig. 3 is in low Reynolds number, and the airflow can separate from the chimney walls and electrical heater surfaces. To reduce computational effort and handle the effects of both low Reynolds number and flow separation, the $k-\omega$ turbulence model was employed here. In the model, the Reynolds stresses $-\rho\overline{u_i' u_j'}$ are calculated by the mean velocity gradients and the eddy viscosity as [41]:

$$-\rho\overline{u_i' u_j'} = \mu_t\left(\frac{\partial u_i}{\partial x_j} + \frac{\partial u_j}{\partial x_i}\right) - \frac{2}{3}\delta_{ij}\left(\rho k + \mu_t\frac{\partial u_k}{\partial x_k}\right) \quad (3)$$

where μ_t is turbulent eddy viscosity, $\mu_t = \rho k/\omega$, ω is turbulent kinetic energy dissipation frequency, δ_{ij} is Kronecker delta.

The steady equations for solving k and ω are written as [41]:

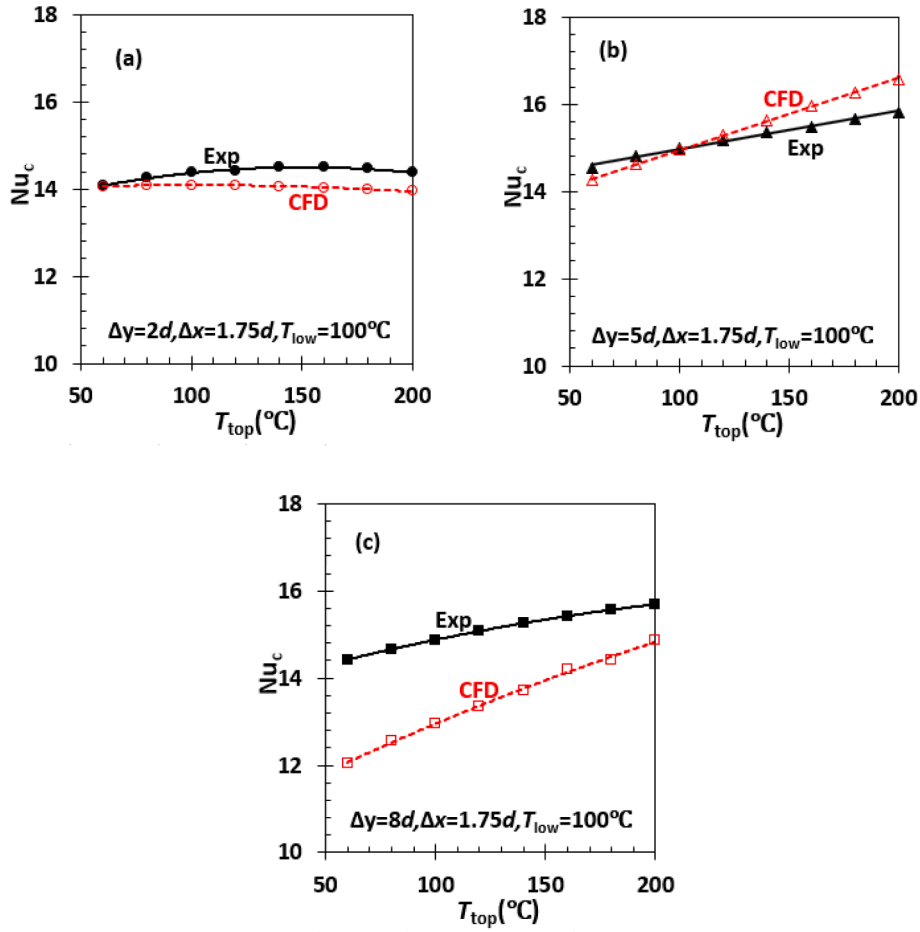

Fig. 9. Experimental convective Nusselt number Nu_c and compared with the Nusselt number predicted by CFD simulations for the low row heaters at$\Delta x = 1.75d$and$T_{low} = 100$ °C, (a) Δy=2d, (b) Δy=5d, and (c) Δy=8d

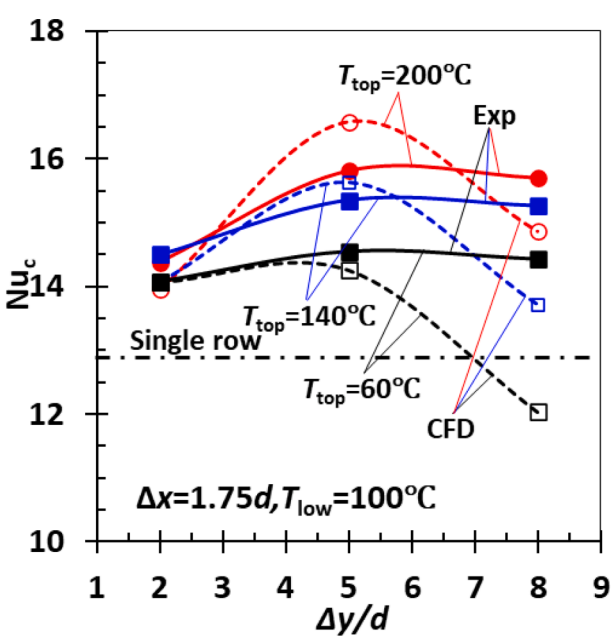

Fig. 10. Experimental and predicted convective Nusselt numbers Nu_c for the low row heaters are plotted as a function of dimensionless centre-to-centre row gap $\Delta y/d$ at$T_{top} = 60$, 140, 200 °C, Δx=1.75d, T_{low}=100 °C.

$$\begin{cases} \dfrac{\partial}{\partial x_j}(\rho u_j k) = \dfrac{\partial}{\partial x_j}\left[\left(\mu + \dfrac{\mu_t}{\sigma_k}\right)\dfrac{\partial k}{\partial x_j}\right] + P_k - \beta_k \rho k \omega + P_{kb} \\ \dfrac{\partial}{\partial x_j}(\rho u_j \omega) = \dfrac{\partial}{\partial x_j}\left[\left(\mu + \dfrac{\mu_t}{\sigma_\omega}\right)\dfrac{\partial \omega}{\partial x_j}\right] + \beta_{\omega 1}\dfrac{\omega}{k}P_k - \beta_{\omega 2}\rho\omega^2 + P_{\omega b} \end{cases} \tag{4}$$

where the model constants $\beta_k = 0.09$, $\beta_{\omega 1} = 5/9$, $\beta_{\omega 2} = 0.075$ and $\sigma_k = \sigma_\omega = 2$ are held. P_k is the turbulence production term, and determined by the mean velocity gradients and given by [41]:

$$P_k = \mu_t\left(\frac{\partial u_i}{\partial x_j} + \frac{\partial u_j}{\partial x_i}\right)\frac{\partial u_i}{\partial x_j} - \frac{2}{3}\frac{\partial u_k}{\partial x_k}\left(3\mu_t\frac{\partial u_k}{\partial x_k} + \rho k\right) \tag{5}$$

The term P_{kb} is the buoyancy production in the k equation, and expressed as $P_{kb} = \rho\beta g_i(\mu_t/\rho\sigma_b)(\partial T/\partial x_i)$, based on the Boussinesq model, σ_b is the turbulent Schmidt number,$\sigma_b = 0.9$. The buoyancy production term $P_{\omega b}$ in the ω equation is expressed as $P_{\omega b} = \omega[(\alpha+1)C_3\max(P_{\omega b}, 0) - P_{kb}]/k$, C_3 is the turbulence dissipation coefficient, $C_3 = 1$ for the Boussinesq model.

$-\rho\overline{u_j'h}$ in Eq. (1) is the Reynolds flux. According to the eddy diffusivity hypothesis, the Reynolds flux is linearly connected with the mean h gradient, i.e. $-\rho\overline{u_j'h} = (\mu_t/\mathrm{Pr}_t)(\partial h/\partial x_i)$, Pr_t is the turbulent Prandtl number, Pr_t=0.85. Because the air velocity in the thermal chimney is slow, three terms P_{kb}, $P_{\omega b}$ and $-\rho\overline{u_j'h}$ are ignored in CFD simulations here.

The boundary layer flows over the heaters and chimney walls should be handled by using very fine mesh generated near the walls. In this context, the dimensionless distance from the walls $y^+ \approx 1$ is kept, where $y^+ = u_\tau y_n/\nu$, u_τ is the friction velocity at the walls, y_n is the distance

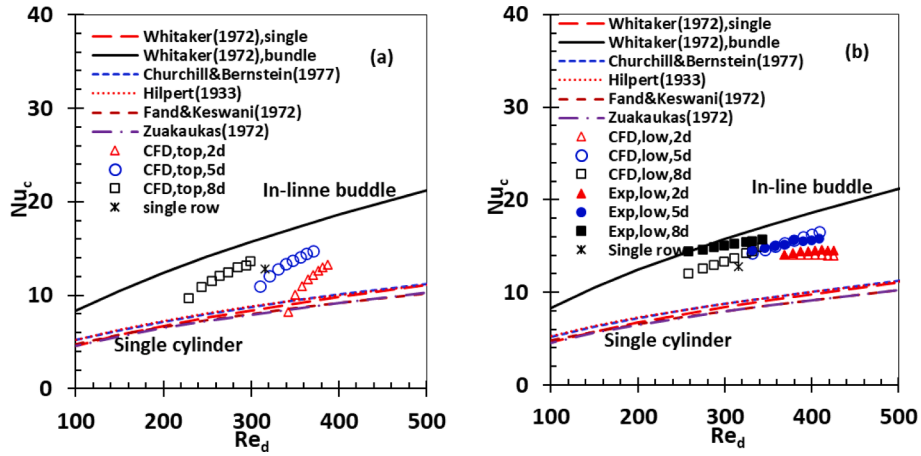

Fig. 11. Convective Nusselt numbers over the top row and low row heaters are compared with the convective Nusselt numbers over single heated cylinder and in-line heated cylinder bundle estimated by employing empirical correlations in the literature, (a) top row, and (b) low row.

Table 4
Summary of existing empirical correlations for convective Nusselt number of flows crossing single heated cylinder and in-line bundle of heated cylinders.

Author	Correlation	Crossflow	Re_d range
Hilpert (1933) [51]	$Nu_c = 0.615Re_d^{0.466}$	single heated cylinder	[40, 4×10^3]
Fand & Keswani (1972) [52]	$Nu_c = 0.184 + 0.324Re_d^{0.5} + 0.291Re_d^{0.247+0.0407Re_d^{0.168}}$		[10^{-2}, 10^5]
Zukauskas (1972) [53]	$Nu_c = 0.51Re_d^{0.5}Pr^{0.37}$		[40, 10^3]
Whitaker (1972) [54]	$Nu_c = \left(0.4\sqrt{Re_d} + 0.06Re_d^{2/3}\right)Pr^{0.4}$		[5, 10^5]
Churchill & Bernstein (1977) [55]	$Nu_c = 0.3 + \frac{0.62Re_d^{1/2}Pr^{1/3}}{\left[1+(0.4/Pr)^{2/3}\right]^{1/4}}\left[1+\left(\frac{Re_d}{28200}\right)^{5/8}\right]^{4/5}$		[0.1, 10^3]
Whitaker (1972) [54]	$Nu_c = \left(0.5\sqrt{Re_d} + 0.2Re_d^{2/3}\right)Pr^{1/3}$	In-line bundle of heated cylinders	[10, 10^5]

Note that the air Prandtl number$Pr = 0.71$ is held.

between the first and second grid points off the walls. The Automatic Near-Wall Treatment in CFX was selected as the wall function to calculate u_τ and ω values at the walls. In the treatment, u_τ and ω at the walls are calculated by means of the blended analytical friction velocity u_τ and ω expressions between the logarithmic-law outer layer and the liner-law viscous sublayer. The lengthy formulas for the velocity u_τ and ω at the walls are referred to [41].

The heat flux at the walls is related to the universal temperature profiles across the viscous sublayer and logarithmic-law outer layer as follows [41]:

$$\begin{cases} T^+ = Pry^+e^{-\Gamma} + \left[0.1\ln y^+ + \left(3.85Pr^{1/3} - 1.3\right) + 0.1\ln Pr\right]e^{-1/\Gamma} \\ \Gamma = \dfrac{0.01(Pry^+)^4}{1+5Pr^3y^+}, T^+ = \dfrac{\rho c_p u_\tau (T_w - T)}{q_w}, Pr = \mu c_p/\lambda \end{cases} \tag{6}$$

where T^+ is the dimensionless temperature, Pr is the Prandtl number of air, T_w and q_w are the temperature at a wall and heat flux through the wall, T is the air temperature near the wall, Γ is auxiliary variable, c_p is the specific heat capacity at constant pressure of air.

Except the natural convective heat transfer, thermal radiation effects exist between the two rows of heaters, and from the heaters to the chimney walls. Since the frequency spectrum information of the radiation and scattering effect on those solid surfaces remain unclear, the grey radiation model has to be accepted here. The grey radiative transfer equation can be written as [41]:

$$I(r,s) = \varepsilon I_b(T_w) + \frac{1-\varepsilon}{\pi}\oiint_{n\cdot s'<0} I(r,s)|n\cdot s'|d\Omega' \tag{7}$$

where $I(\boldsymbol{r},\boldsymbol{s})$ is the radiation intensity at wall, $\boldsymbol{r}$ is the radius vector of a point on solid surface or wall, $\boldsymbol{s}$ is thermal radiation direction at wall, $\boldsymbol{n}$ is outwards normal vector of wall, s' is the dummy variable in the integral, Ω' is the dummy variable of solid angle Ω, $\boldsymbol{n} \bullet s' < 0$ means the reflection of the thermal radiation from a solid surface or wall, I_b is the black body radiation intensity. Eq. (7) is solved for $I(\boldsymbol{r},\boldsymbol{s})$ by tracking a number of thermal radiation rays with the discrete transfer method. $I_b(T_w)$ is the blackbody thermal radiation intensity emitted from a solid surface and determined by [41]:

$$I_b(T_w) = \sigma T_w^4 \tag{8}$$

where σ is the Stefan-Boltzmann constant.

2.3. Boundary conditions

Most of the boundary conditions have been demonstrated in Fig. 3. There are two symmetrical boundary conditions in each fluid domain. Further, there are two fluid–fluid interfaces between domain 1 and domain 2, and between domain 2 and domain 3. In domain 1, the ground floor is opaque, no-slip and smooth wall with 10 ℃ temperature and 0.95 emissivity, the rest two surfaces are opening boundary condition where zero relative pressure, velocity normal to the surface, 5% turbulence intensity, 20 ℃ opening temperature and 20 ℃ external blackbody (far field ambient) temperature are given.

In domain 2, except the two symmetrical conditions, there are two no-slip, opaque, smooth chimney walls with 20 ℃ and 0.94 emissivity. Additionally, there are five no-slip, opaque, smooth walls for the top and low heater surfaces. The top row and low row heater surfaces are subject to 0.27 emissivity and different wall heat fluxes. The heat fluxes across the top row and low row heater surfaces are assigned based on a trial-and-error manner by using the bi-section method until the averaged wall temperatures in a CFD simulation have matched the experimental surface temperatures within ± 0.3 ℃ tolerance.

In domain 3, there are two surfaces in opening boundary condition

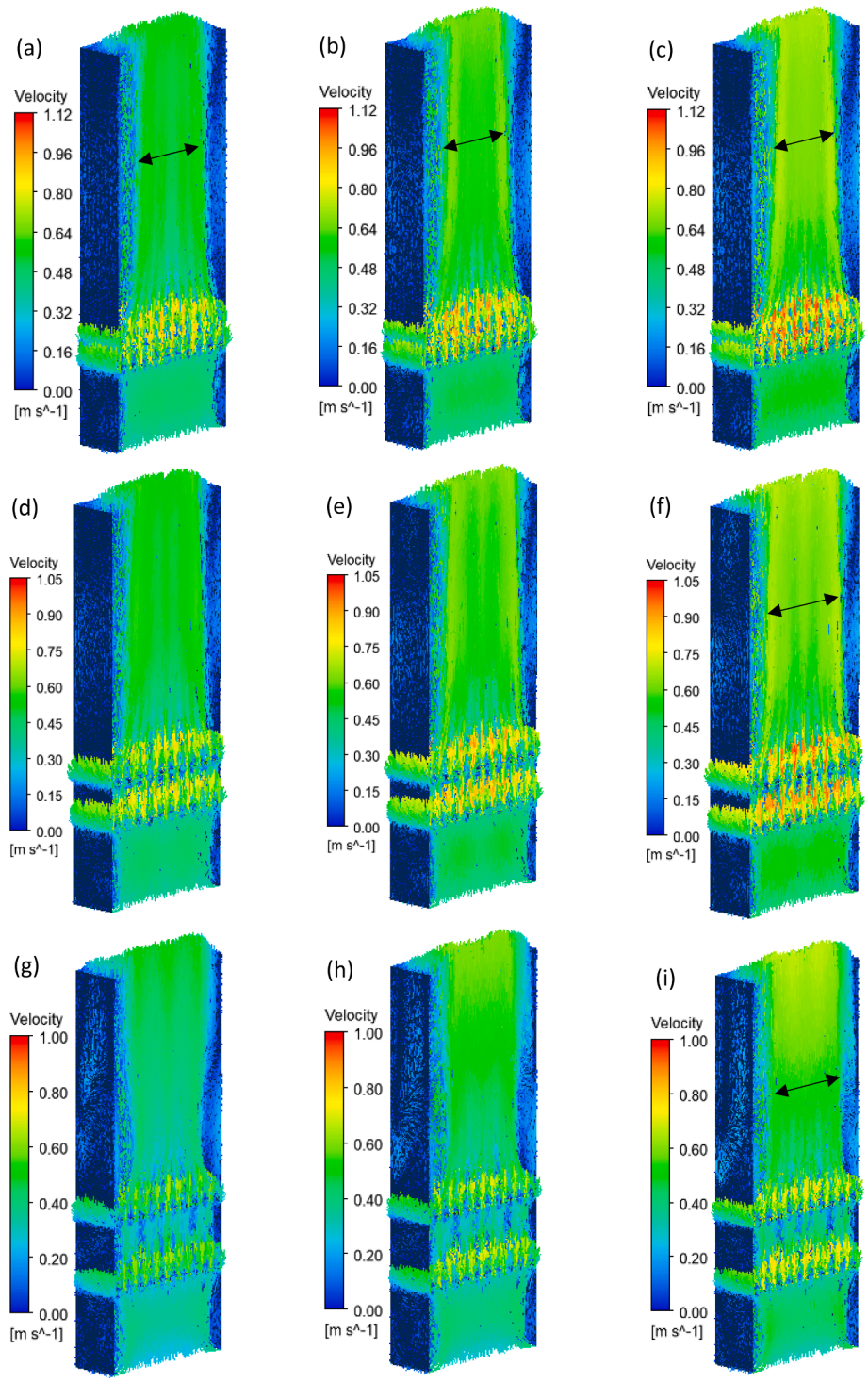

Fig. 12. 3D plots of air velocity in the half chimney with two row heaters at $\Delta y = 2d$, $5d$, $8d$ and $\Delta x = 1.75d$, the top row heaters are at 80, 140 and 200 ℃ nominal temperatures, but the low row heaters are at 100 ℃ nominal temperature, (a)-(c) for$\Delta y = 2d$, (d)-(f) for$\Delta y = 5d$, (g)-(i) for$\Delta y = 8d$, (a), (d) and (g) at 80 ℃, (b), (e) and (h) at 140℃, (c), (f) and (i) at 200 ℃, the lines with two arrows indicate core flow size.

where zero relative pressure, velocity normal to the surface, 5% turbulence intensity, 20 ℃ opening temperature and 20 ℃ external blackbody (far field ambient) temperature are imposed. At the exit of the domain, there is one outlet boundary condition where zero static pressure and local temperature option for thermal radiation are specified.

In the simulations, the high-resolution scheme and 2nd-order scheme are applied in the advection/convection and diffusion terms in Eqs. (1) and (4), respectively. The maximum iteration number is 200 and the residual target for all the variables is 10^{-6} in terms of root-mean-square error. The velocities in the centres of the inlet and outlet of the chimney are recorded and monitored. It is shown that these velocities remain unchanged after 150 iterations. In the discrete transfer method, the number of thermal radiation rays per mesh element is 8, and the radiative transfer equation Eq. (7) is coupled once with the momentum, energy and turbulence model equations Eqs. (1) and (4) at every 10 iterations.

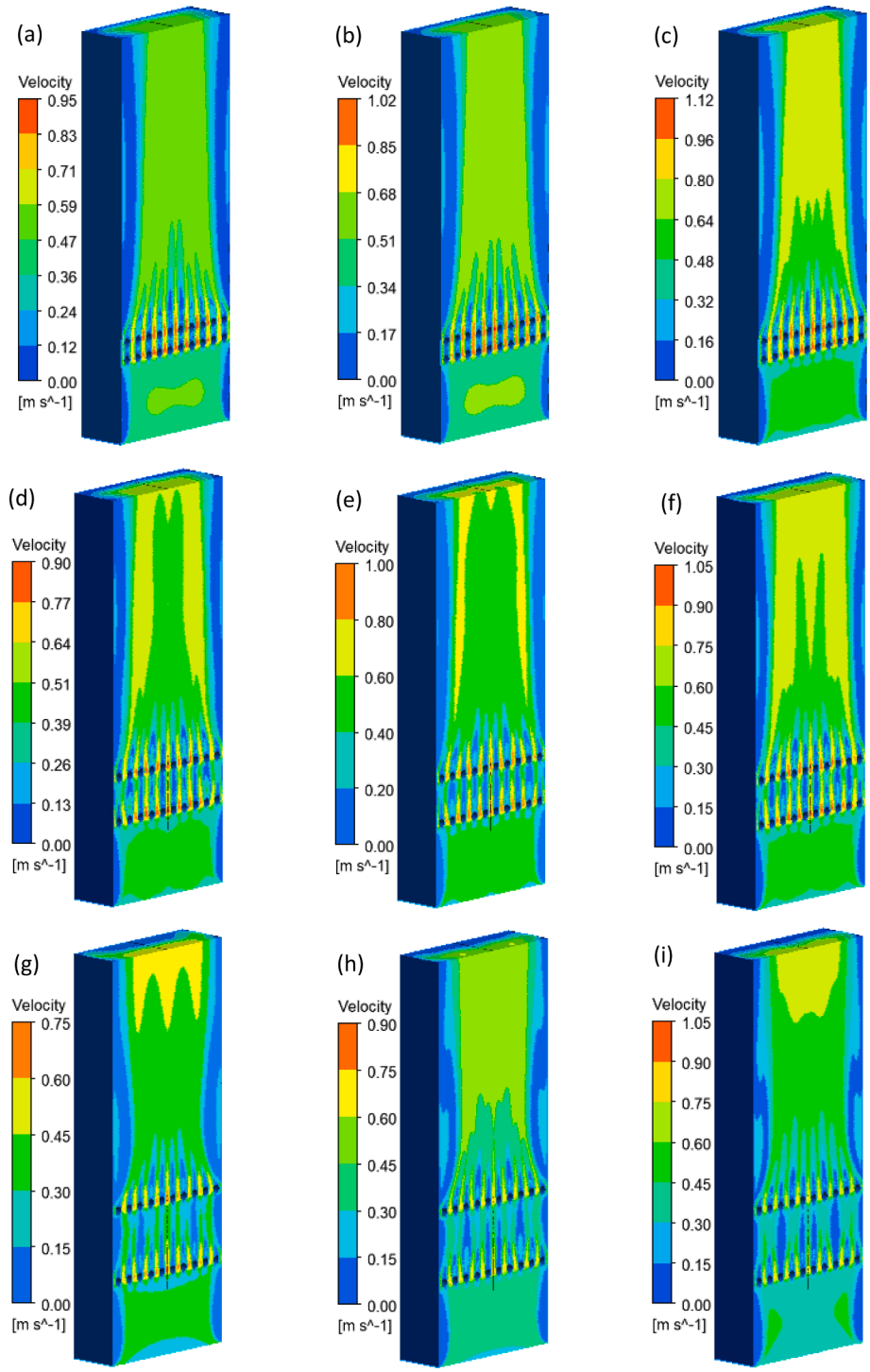

Fig. 13. Contours of air velocity in the half chimney with two row heaters atΔy = 2d, 5d, 8d andΔx = 1.75d, the top row heaters are heated at 80, 140 and 200 ℃ nominal temperatures, but the low row heaters at 100 ℃ nominal temperature, (a)-(c) for$\Delta y = 2d$, (d)-(f) for$\Delta y = 5d$, (g)-(i) for$\Delta y = 8d$, (a), (d) and (g) at 80℃, (b), (e) and (h) at 140 ℃, (c), (f) and (i) at 200 ℃.

2.4. Mesh size independence and velocity validation

Three meshes, i.e., Mesh 1, Mesh 2 and Mesh 3, were generated in ANSYS Meshing module in the case of$\Delta y = 5d$to check mesh size independence. A mesh closed-up is illustrated in Fig. 3. The information about mesh or element size, type of elements, number of nodes, number of elements, mesh quality, dimensionless distance from wall and energy gain coefficient are listed in Table 3. The chimney energy gain coefficient η_{th} is defined as the ratio of the air energy rise between the chimney inlet and outlet to the thermal energy input from the heaters in the two rows:

$$\eta_{th} = \frac{m_f c_p \left(T_{f2} - T_{f1}\right)}{NA\left(q_{top} + q_{low}\right)} \tag{9}$$

where m_f is the air mass flow rate through the chimney, T_{f1} and T_{f2} are the air temperatures at the chimney inlet and outlet, respectively; A is the area of the surface of a heater exposed to the inner air body, $A=\pi dl$, d

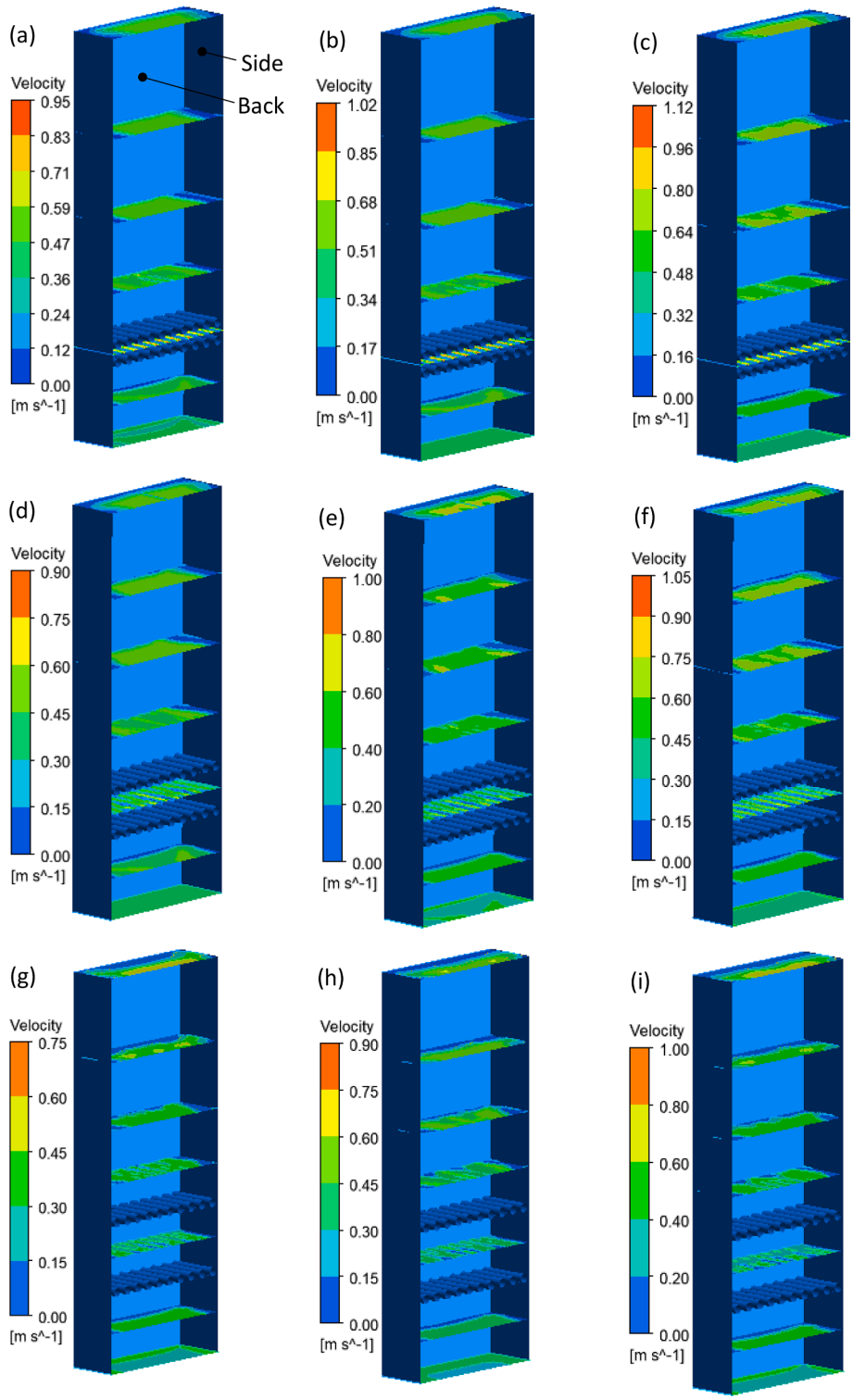

Fig. 14. Cross-sectional contours of air velocity in the half chimney with two row heaters at$\Delta y = 2d$, $5d$, $8d$ and$\Delta x = 1.75d$, the top row heaters are at 80, 140 and 200 ℃ nominal temperatures, while the low row heaters at 100 ℃ nominal temperature, (a)-(c) for$\Delta y = 2d$, (d)-(f) for$\Delta y = 5d$, (g)-(i) for$\Delta y = 8d$, (a), (d) and (g) at 80 ℃, (b), (e) and (h) at 140 ℃, (c), (f) and (i) at 200 ℃.

is the heater diameter, d=16 mm, l is the heater length exposed to the air, l=190 mm, q_{top} is the given wall heat flux through the surface of a heater in the top row, q_{low} is the given wall heat flux across the surface of a heater in the low row, N is the number of heaters in the top or low row, N=10. Parameters m_f, T_{f1}, and T_{f2} are extracted from CFD simulation result files. Note that the quantity $1 - \eta_{th}$ is the thermal energy loss coefficient through the chimney walls and ground floor, and the corresponding thermal energy loss through the ground floor and chimney walls is$Q_L = NA\left(q_{top} + q_{low}\right) - m_f c_p \left(T_{f2} - T_{f1}\right)$.

The curves of y^+ of the heaters in the top and low rows and energy gain coefficient η_{th} versus number of elements of Mesh 1, 2 and 3 are illustrated in Fig. 5. Generally, the dimensionless distance $y^+ \approx 1$ is reached at three mesh sizes. Further, Mesh 1 leads to a larger η_{th} than

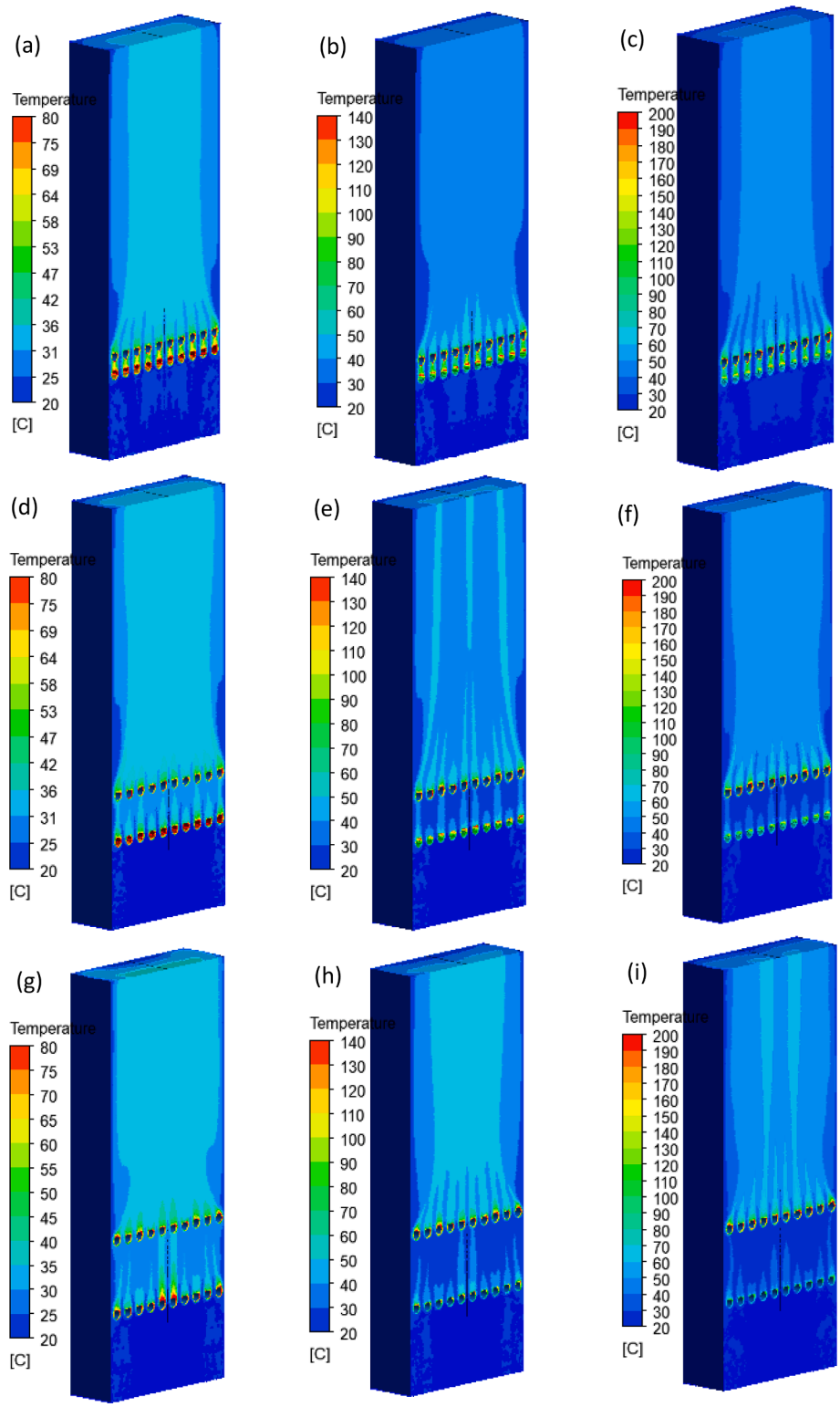

Fig. 15. Contours of air temperature in the half chimney with two row heaters at$\Delta y = 2d$, $5d$, $8d$ and$\Delta x = 1.75d$, the top row heaters are operated at 80, 140 and 200℃ nominal temperatures, but the low row heaters at 100 ℃ nominal temperature, (a)-(c) for$\Delta y = 2d$, (d)-(f) for$\Delta y = 5d$, (g)-(i) for$\Delta y = 8d$, (a), (d) and (g) at 80 ℃, (b), (e) and (h) at 140 ℃, (c), (f) and (i) at 200 ℃.

Mesh 2 and Mesh 3. η_{th} varies as little as 0.0018 when the mesh is changed to Mesh 3 from Mesh 2. This fact suggests that the mesh size independency is achieved at Mesh 2 and Mesh 3, thus, the results at Mesh 2 will be showed in the in following sections. A similar result is obtained in the cases of$\Delta y = 2d$and $8d$ and omitted here.

The velocity profile predicted by ANSYS CFX has been validated by employed PIV measurements in the thermal chimney with single row heaters [39]. The PIV measurements were performed in the mid-span plane across the heaters in the chimney at three heater temperatures: T_{low}=80, 120, 160 ℃. The errors in the mean velocity between PIV and CFD are ranged in (-30- + 2) % at the three heat temperatures. The details of the validation are described in Appendix A.

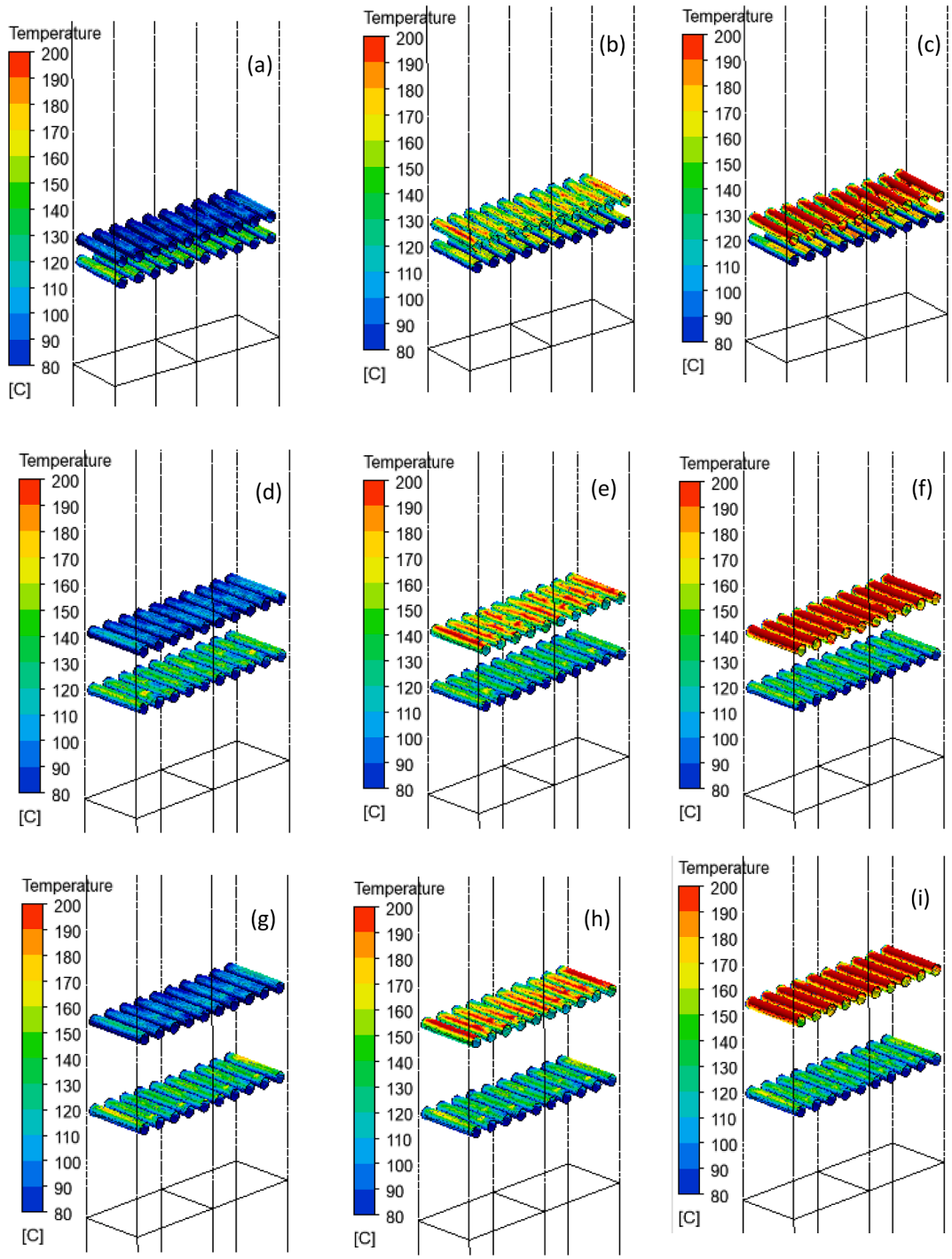

Fig. 16. Contours of surface temperature of two row heaters at$\Delta y = 2d$, $5d$, $8d$ and$\Delta x = 1.75d$, the top row heaters are at 80, 140 and 200 ℃ nominal temperatures, but the low row heaters at 100 ℃ nominal temperature, (a)-(c) for$\Delta y = 2$d, (d)-(f) for$\Delta y = 5d$, (g)-(i) for$\Delta y = 8d$, (a), (d) and (g) at 80 ℃, (b), (e) and (h) at 140 ℃, (c), (f) and (i) at 200 ℃.

3. Results

3.1. Overall thermal performance

Overall thermal performance of the thermal chimney consists of temperature rise of air ΔT_f, dimensionless mass flow rate of the air through the chimney m_f/m_{f0}, energy gain coefficient of the chimney η_{th}, Reynolds number around the heaters Re_d, Reynolds number of the chimney Re and thermal power of the low row heaters P_{low} when the nominal temperature of the top row heaters varies but the nominal temperature of the low row heaters is fixed atT_{low} = 100 ℃. These performance parameters are illustrated in Fig. 6 in terms of nominal temperature of the top row heaters T_{top} at Δx=1.75d, andΔy = 2d, 5d, 8d. The Reynolds number around the heaters Re_d, Reynolds number of the chimney Re are defined as:

$$\mathrm{Re}_d = \frac{u_f d}{\nu}, Re = \frac{u_f d_h}{\nu}, u_f = \frac{1}{2}\left(u_{f1} + u_{f2}\right), d_h = \frac{4ab}{2(a+b)} \tag{10}$$

where u_f is the air characteristic or bulk velocity, u_{f1} and u_{f2} are the air velocity at the inlet and outlet of the chimney, respectively; d_h is the

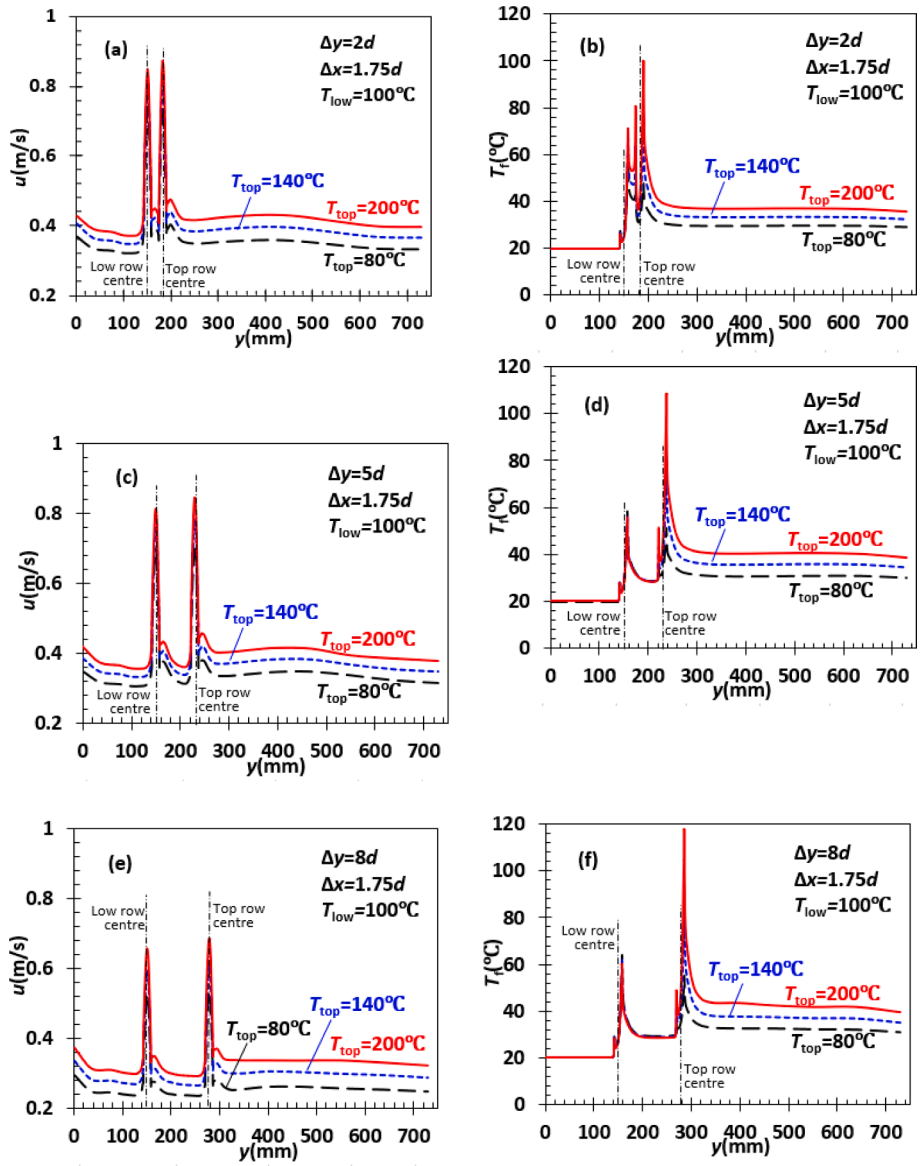

Fig. 17. Cross-sectional mean air velocity and temperature along the flow path in the chimney with two row heaters at$\Delta y = 2d$, $5d$, $8d$ and$\Delta x = 1.75d$, the top row heaters are heated at 80, 140 and 200 ℃ nominal temperatures, but the low row heaters at 100 ℃ nominal temperature, (a) and (b) for$\Delta y = 2d$, (c) and (d) for$\Delta y = 5d$, (e) and (f) for$\Delta y = 8d$.

hydraulic diameter of the chimney, a and b are the width and depth of inner cross-section of the chimney, a=280 mm, b=190 mm, ν is the air kinematic viscosity and calculated by:

$$\nu = \frac{\mu}{\rho}, \mu = \frac{1.4592 \times 10^{-6} T_f^{1.5}}{109.1 + T_f}, \rho = \frac{351.99}{T_f} + \frac{344.84}{T_f^2} \tag{11}$$

where T_f is the bulk temperature of the air in the chimney, $T_f = 0.5(T_{f1} + T_{f2})$. The expressions of both ρ and μ are after [43].

In Fig. 6(a), the temperature rise of the air ΔT ascends linearly with increasing temperature of the top row heaters T_{top}. At a fixed T_{top}, ΔT rises with increasing Δy, but the increment in ΔT becomes saturated as$\Delta y \geq 5d$. Compared with the ΔT in the chimney with single row heaters predicted in [39], the ΔT in the chimney with two row heaters are almost doubled in magnitude at$T_{top} = 100$ ℃. Thus, the top row heaters installed are favourable for improvement of air temperature rise.

In Fig. 6(b), the dimensionless air mass flow rate m_f/m_{f0} rises linearly with T_{top}, where m_{f0} is the air mass flow rate in the chimney with single row heaters at 100 ℃ [39], m_f is the air mass flow in the chimney with two row heaters herein. At a fixed T_{top}, m_f/m_{f0} decreases with increasing Δy; interestingly, the m_f/m_{f0} at$\Delta y = 8d$ is smaller than the m_f/m_{f0} in the chimney with single row heaters at 100 ℃.

In Fig. 6(c), the energy gain coefficient η_{th} decreases with increasing T_{top}. At$\Delta y = 5d$the chimney shows the best energy gain coefficient atT_{top} greater than 110 ℃. At$\Delta y = 2d$and $5d$ the η_{th} is better than the η_{th} of the chimney with single row heaters at 100 ℃ [39]. At$\Delta y = 8d$, however, the η_{th} is poorer than the η_{th} of the latter.

In Fig. 6(d) and (e), the Reynolds number around heaters Re_d and the Reynolds number of the chimney Re rise as T_{top} increases. Re_d and Re share nearly the same trend against T_{top}. The difference in Re_d and Re magnitudes depends on the ratio of the heater diameter to the hydraulic diameter of the chimney.

The experimental electrical power of one heater in the low row in the chimney is illustrated in Fig. 7 and compared with the thermal power calculated in CFD simulations by using the known wall heat fluxes. Generally, the experimental electrical power is higher than the thermal power calculated, especially at$\Delta y = 8d$. The two power values are close to each other at$\Delta y = 5d$. At Δy=$2d$, however, the two power values

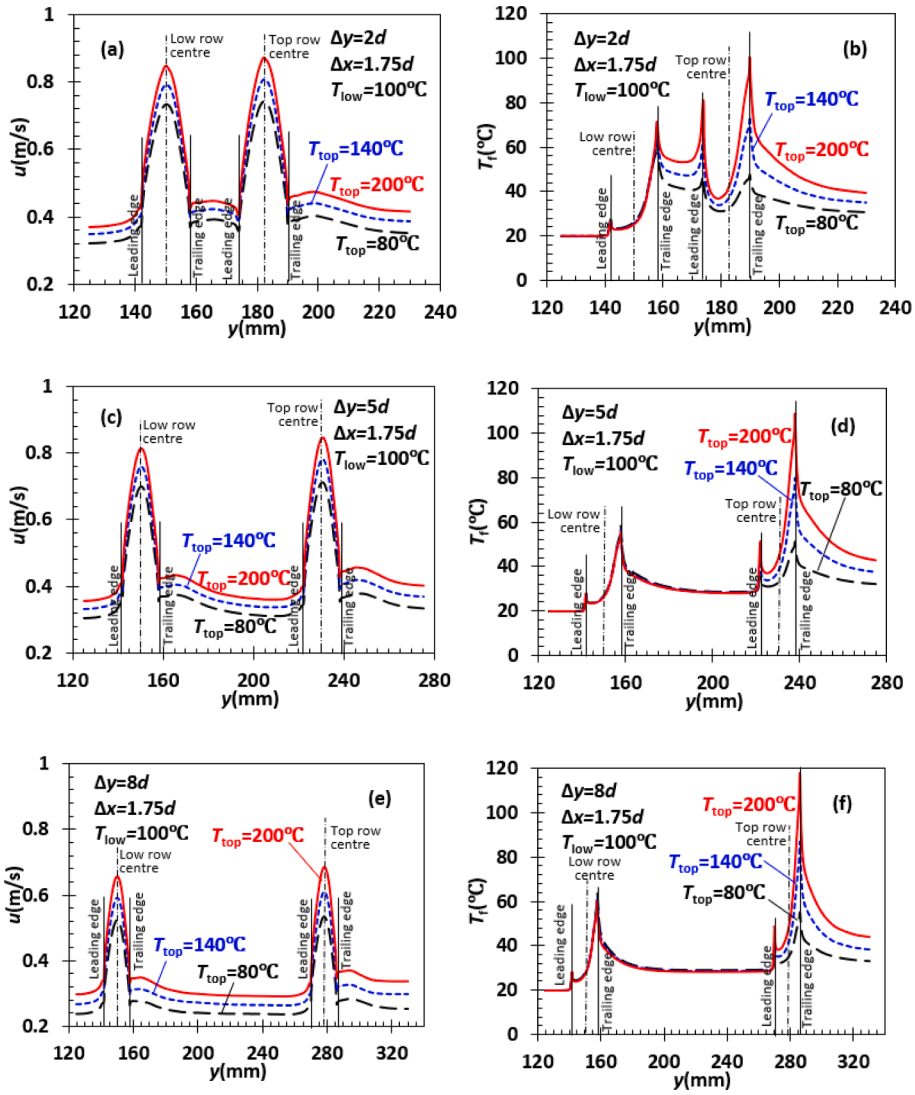

Fig. 18. Localised cross-sectional mean air velocity and temperature along the flow path in the chimney with two row heaters at$\Delta y = 2d$, $5d$, $8d$ and$\Delta x = 1.75d$, the top row heaters are heated at 80, 140 and 200 ℃ nominal temperatures, but the low row heaters at 100 ℃ nominal temperature, (a) and (b) for$\Delta y = 2d$, (c)-and (d) for$\Delta y = 5d$, (e) and (f) for$\Delta y = 8d$.

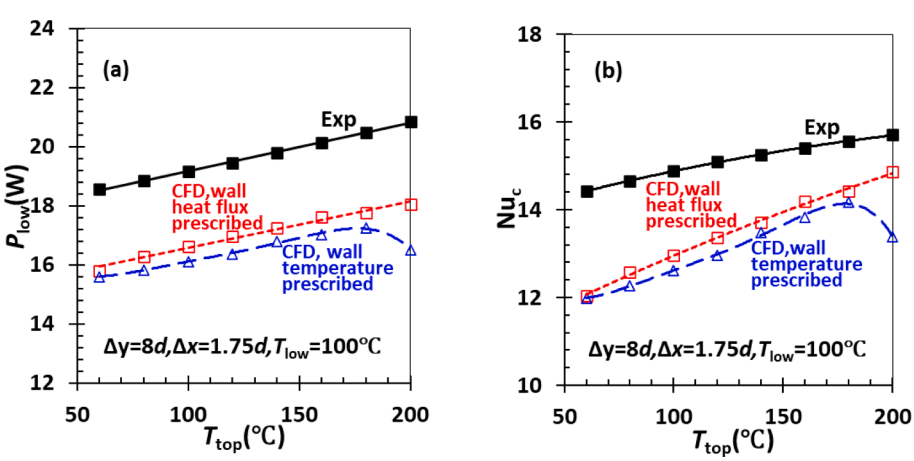

Fig. 19. Experimental electrical power of one heater in the low row (a) and convective Nusselt number (b) are compared with the thermal power and convective Nusselt number calculated in CFD simulations at$\Delta y = 2d$, $5d$, $8d$ and fixed$\Delta x = 1.75d$, T_{low}=100 ℃, Exp-experimental data.

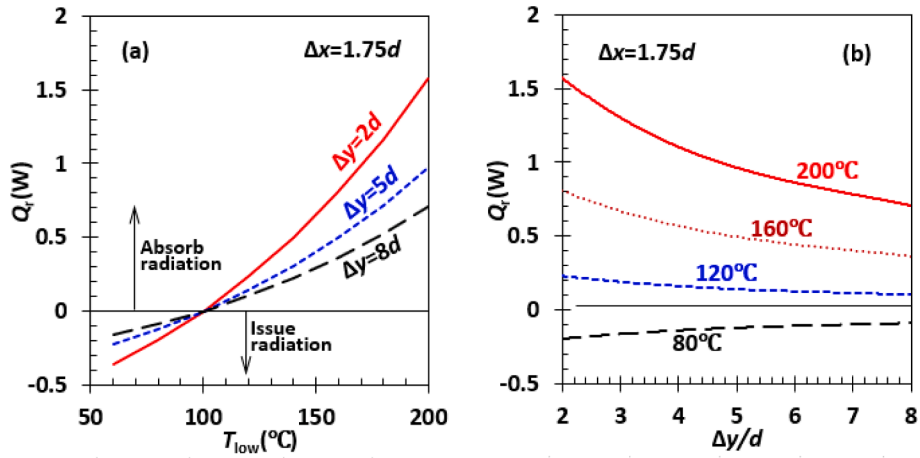

Fig. 20. Mean thermal radiation power from the top row heaters to the low row heaters, which was estimated by using Eqs. (14) and (15), (a) power vs temperature at $\Delta y = 2d$, $5d$, $8d$, (b) power vs $\Delta y/d$ at 80, 120, 160, 200 °C.

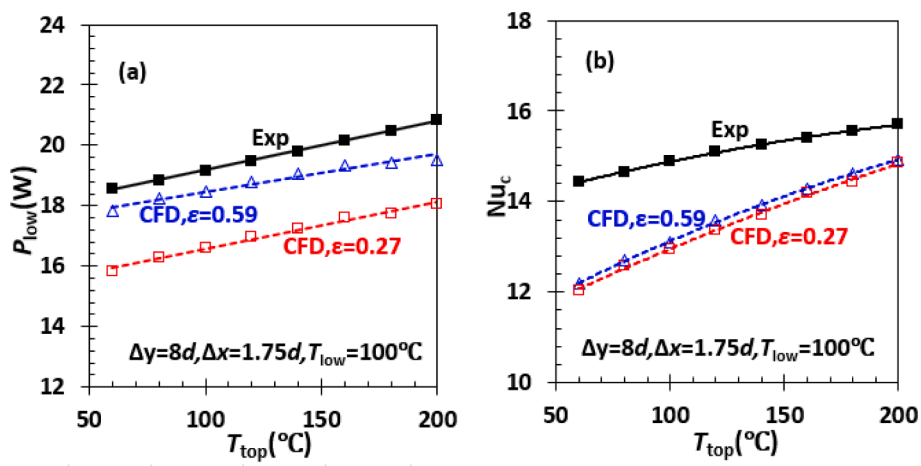

Fig. 21. Thermal power and convective Nusselt number predicted with two different emissivity values, (a) thermal power, (b) convective Nusselt number.

exhibit a reverse trend against T_{top}. The slope of these curves gets steeper with increasing Δy. This effect is attributed to the thermal radiation of the top row heaters to the low row heaters and details about the thermal radiation from the top row heaters to the low row heaters and emissivity of the heater surfaces will be discussed in Section 4.2.

3.2. Heat transfer characteristics

The heat transfer characteristics of the low row heaters in the chimney are mainly described by using convective Nusselt number Nu_c, radiative equivalent Nusselt number Nu_r and total Nusselt number Nu_t, which are related to the corresponding convective, radiative and total heat transfer coefficients over the low row heaters, heater diameter and air thermal conductivity, respectively. The convective Nusselt number Nu_c, radiative equivalent Nusselt number Nu_r are calculated by using wall convective heat flux q_c and radiative heat flux q_r with the following expressions:

$$\mathrm{Nu}_c = \frac{q_c d}{\lambda\left(T_{low} - T_f\right)}, \mathrm{Nu}_r = \frac{q_r d}{\lambda\left(T_{low} - T_f\right)}, \mathrm{Nu}_t = \mathrm{Nu}_c + \mathrm{Nu}_r, \lambda = \frac{2.3340 \times 10^{-3} T_f^{1.5}}{164.54 + T_f} \tag{12}$$

where q_c and q_r are the wall convective and radiative heat fluxes over the low row heaters, q_c=q_t-q_r, q_t is a given wall heat flux, q_r is calculated in CFD simulations, the expression of λ is taken from [43]. The definition and use of radiative equivalent Nusselt number can be found in [44–50] and are followed in the paper to facilitate the comparison between radiative heat transfer and convective heat transfer quantitively. The convective Nusselt number Nu_c, radiative equivalent Nusselt number Nu_r and total Nusselt number Nu_t of the low row heaters calculated with CFD simulation results are illustrated in Fig. 8.

The convective Nusselt number Nu_c reduces at$\Delta y = 2d$but rises at$\Delta y = 5d, 8d$with increasing T_{top}. The Nu_c values are greater than the Nu_c value of the single row heaters presented in [39]. Obviously, the top row heaters have enhanced the convective heat transfer over the low row heaters in comparison with that over the single row heaters. The$\Delta y = 5d$ results in the highest Nu_c, thus the strongest heat transfer enhancement.

The radiative equivalent Nusselt number Nu_r declines at$\Delta y = 2d$but grows at$\Delta y = 5d, 8d$with increasing T_{top}. The Nu_r values at Δy=$2d$, $5d$, $8d$ are about (30–40)% of the Nu_r value of the single row heaters. Hence, the top row heaters apparently have suppressed the thermal radiation issued from the low row heaters.

The variation trend of the total Nusselt number Nu_t resembles that of the convective Nusselt number Nu_c at each Δy. The Nu_t values at$\Delta y = 2d, 5d, 8d$are smaller than the Nu_t value of the single row heaters. Overall, the top row heaters seem to enhance the convective heat transfer and reduce the thermal radiation of the low row heaters.

The experimental convective Nusselt number Nu_c is compared with the convective Nusselt number predicted in CFD simulations at$\Delta y = 2d, 5d, 8d$in Fig. 9. The predicted convective Nusselt number shares a similar

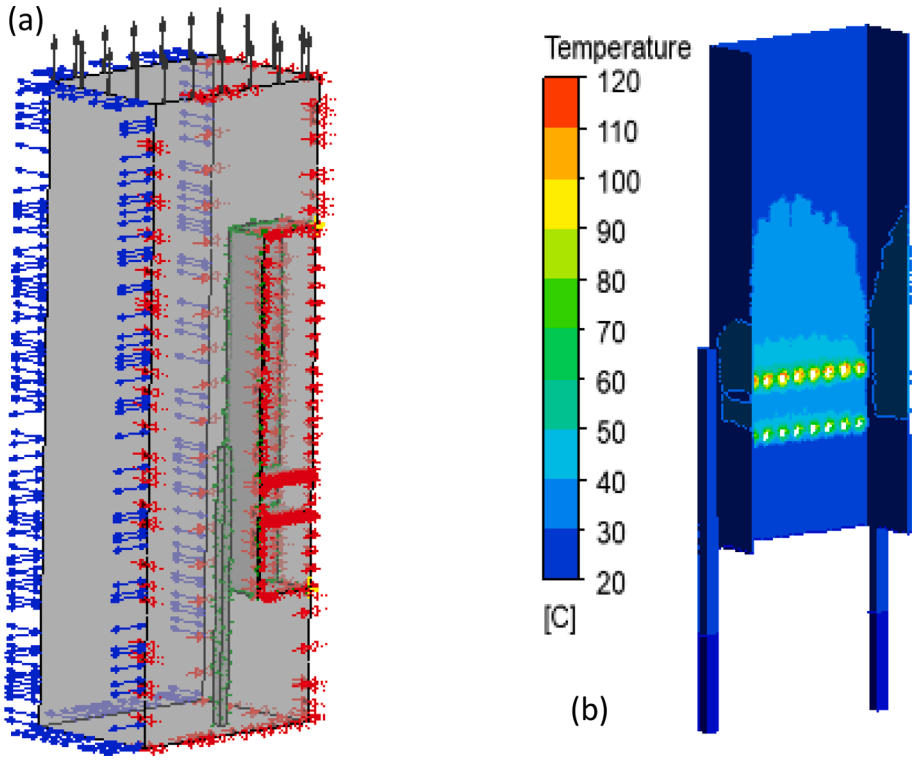

Fig. 22. Complex fluid–solid domain (a), temperature contour on the chimney walls (b)under the conditions: Δy=5d, T_{low}=100℃CandT_{top} = 140℃.

variation trend against T_{top} with the experimental convective Nusselt number. Interestingly, the predicted convective Nusselt number agrees well with the experimental convective Nusselt number at$\Delta y = 2d, 5d$. However, the agreement between experiment and prediction in convective Nusselt number is poor at$\Delta y = 8d$. This fact suggests that the flow and heat transfer models have underestimated the influence of the top row heaters upon the low row heaters.

Note that the convective Nusselt number is the highest at$\Delta y = 5d$. The experimental and predicted convective Nusselt numbers are presented as a function of $\Delta y/d$ atT_{top} = 60, 140, 200 ℃, Δx=1.7 5d, T_{low}=100 ℃ in Fig. 10. The experimental convective Nusselt number profiles indicate that the highest Nusselt number occurs at Δy=(5 − 6)d. The convective Nusselt number profiles predicted by using CFD simulations demonstrate that the highest Nusselt number is located atΔy = 5d. Based on these profiles, Δy=5d is the optimal design for the thermal chimney with heaters in two rows forΔx = 1.75d configuration.

Finally, the convective Nusselt numbers of the low row and top row heaters are compared in Fig. 11 with the convective Nusselt numbers of single heated cylinder and in-line bundle of heated cylinders determined by using six existing empirical correlations found in the literature, which are tabulated briefly in Table 4. The convective Nusselt number of the top row heaters was calculated with Eq. (12) but T_{low} was replaced with T_{top}.

The five correlations for single heated cylinder lead to almost identical convective Nusselt number Nu_c at a given Reynolds number Re_d. The Nu_c value of the top row heaters shows a greater change with increasing Re_d, but is in the middle between the Nu_c curves of in-line cylinder bundle and single cylinder, especially at Δy=5d, 8d. The Nu_c value atΔy = 5$d$is the highest, and the Nu_c atΔy = 2d is the smallest, and even below the Nu_c of single cylinder atRe_d < 350.

Generally, the Nu_c value of the low row heaters is greater than the Nu_c value of the top row heaters. The Nu_c value of the low row heaters demonstrates a less change with increasing Re_d, and is near the Nu_c curve of in-line cylinder bundle at Δy=5d, 8d but in the middle between the Nu_c curves of in-line cylinder bundle and single cylinder atΔy = 2d. The Nu_c value atΔy = 5$d$is the largest, but the Nu_c atΔy = 2d is the lowest.

The Nu_c value of the case with single row heaters is comparable to the Nu_c value of the top row heaters, but inferior to the Nu_c values of the low row heaters, especially atΔy = 5d. This effect implies that there is an enhancement in convective heat transfer over the low row heaters by the intensified upward air draft which is resulted mainly by the top row heaters, and the corresponding maximum enhancement in Nu_c is (11.6–29.8) %, depending on Re_d.

3.3. Flow and temperature details

The vectors and contours of air velocity in the chimney are illustrated in Fig. 12 and Fig. 13, respectively, as the top row heaters are at 80, 140 and 200 ℃ nominal temperatures and the low row heaters is at 100 ℃ nominal temperature. The air is enforced to flow into the chimney with nearly uniform velocity under the action of buoyancy effect. Then, it passes through the gaps between the heaters in the low and top rows as multiple jets. At Δy=2d, the jets don't mix each other until leaving the top row heaters. At Δy=5d, the jets enter the top row as soon as they start to mix each other after leaving the low row heaters. At Δy=8d, however, the jets already have mixed each other after leaving each row heaters.

The boundary layers are built up on the chimney walls as soon as the air enters the chimney. The thinnest boundary layer or the largest size core flow, is observed atΔy = 5d at three nominal temperatures. The boundary layer thickness or core flow size seems to change a little with increasing nominal temperature of the top row heaters.

The air velocity contours in seven cross-sections including the inlet and outlet of the chimney are shown in Fig. 14 when the top row heaters work at 80, 140 and 200 ℃ nominal temperatures and the low row heaters operate at 100 ℃ nominal temperature. The thickest boundary layers are found on the side walls atΔy = 2$d$and 5d, but on the back walls atΔy = 8d. This suggests that the largest velocity deficiency and the poorest thermal performance should take place atΔy = 8d.

The air temperature contours in the chimney are demonstrated in Fig. 15 when the top row heaters are at 80, 140 and 200 ℃ nominal

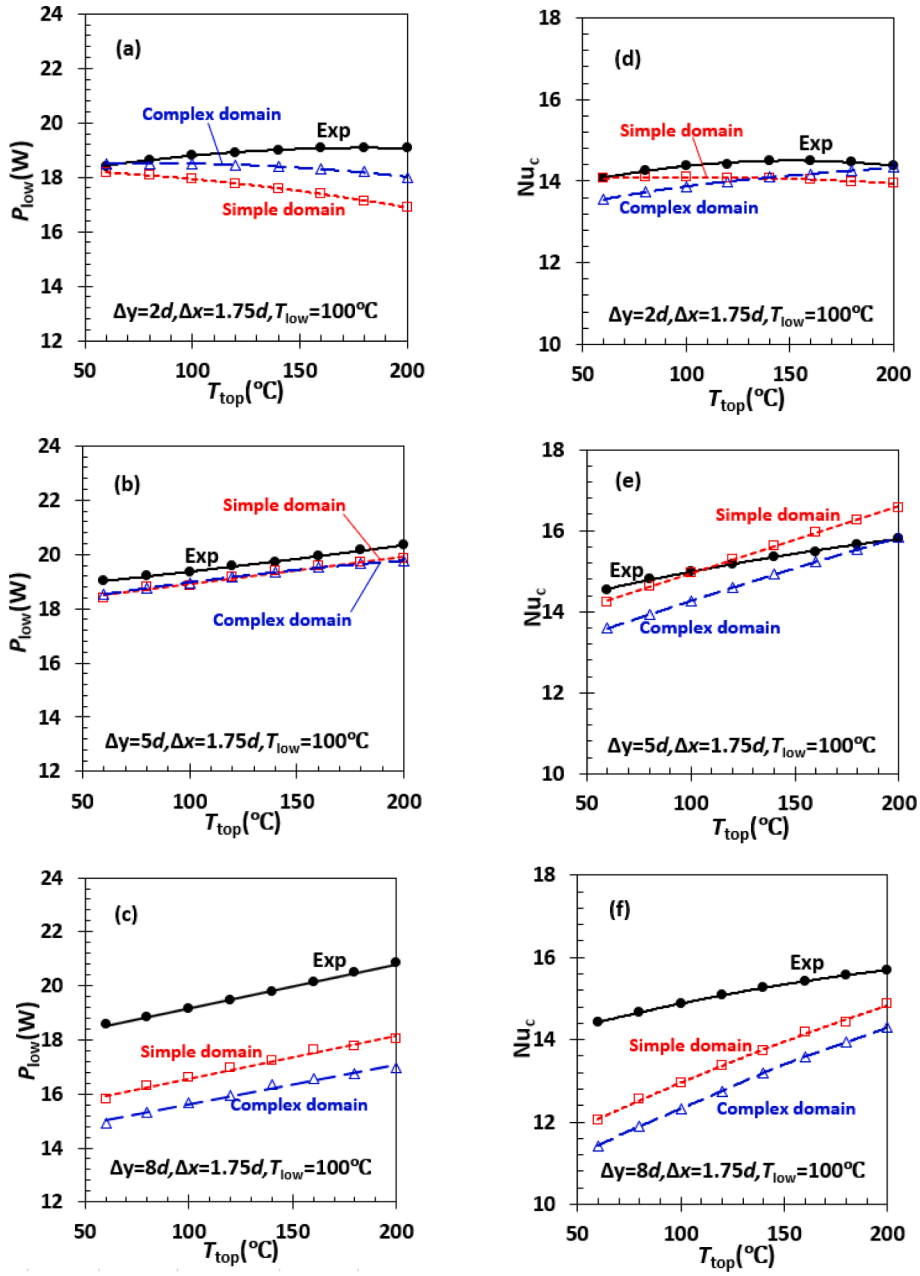

Fig. 23. Thermal powers and convective Nusselt numbers predicted with the complex solid–fluid domain and simple domain for the low row heaters, (a)-(c) thermal power, (d)-(f) convective Nusselt number.

temperatures and the low row heaters is at 100 ℃ nominal temperature. There are thermal boundary layers in every case and the core flow is in a higher temperature. The air temperature is the highest in the wake of each heater. Since the top row heaters are the closest to the chimney outlet, the air temperature at the outlet is the highest at Δy=8d, then followed atΔy = 5$d$and 2d, respectively. The most significant variation in air temperature is identified near every heater, and the air temperature exhibits the smallest variation in the core flow.

The contours of temperature on the surfaces of the low and top row heaters are present in Fig. 16 at Δy=2d, 5d and 8d, as the top row heaters at 80, 140 and 200 ℃ nominal temperatures and the low row heaters at 100 ℃ nominal temperature. Although a uniform heat flux was given to the heaters in each row in CFD simulations, the predicted temperature on each heater surface is nonuniform. Additionally, the windward side of a heater is subject to a higher temperature than the leeward side.

The cross-sectional averaged air velocity and temperature along the flow path, i.e. the y direction as shown in Fig. 3, are illustrated in Fig. 17 for a general trend and in Fig. 18 for a localised view. The air flows towards the heaters in each row in a certain deacceleration. When the air passes through these heaters, its velocity experiences the maximal value at the throat in the gap between two heaters in a row. After the air leaves from the top row heaters, its velocity starts to drop off signicantly, then silighly increases until y≈400 mm due to the narrowest core flow size or the thickest boundary layers on the side walls of the chimney as shown in Fig. 12 and Fig. 13, from there the velocity levels off untill the exit of the chimney. The maximum of the velocity depends on the heater nominal temperature; and the higher the temperature, the larger the maximum.

The air temperature experiences two peaks at the leading and trailing edges of the heaters as passing through the gaps among the heaters in each row. The air temperature exhibits a jump after leaving from each row of heaters, and then remains declined until the outlet of the

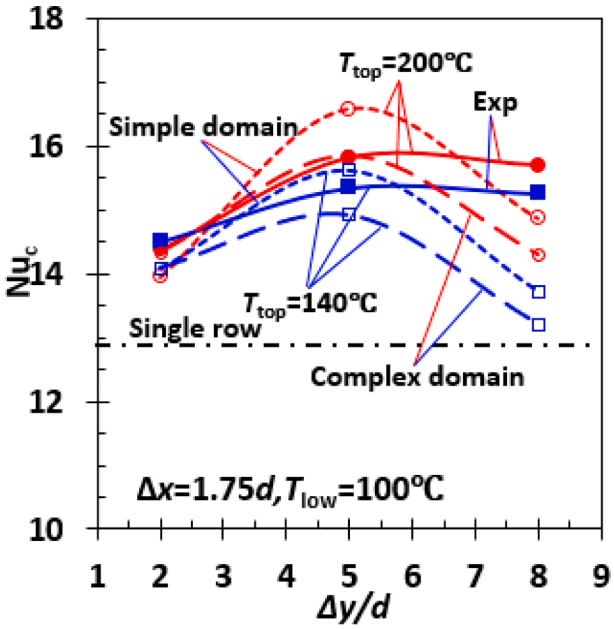

Fig. 24. Convective Nusselt numbers predicted with the complex solid–fluid domain and simple domain are compared with the experimental Nusselt numberfor the low row heaters atT_{top} =140, 200 ℃ andT_{low} = 100 ℃.

chimney. The temperature jump relates to the heater nominal temperature; and the higher the nominal temperature, the larger the temperature jump.

4. Discussion

In this paper, CFD simulation and experiment on convective heat transfer in a 3D thermal chimney with two row heaters were conducted to clarify the chimney thermal performance, and fluid flow and temperature details at a number of heater nominal temperatures ranged 60–200 °C in the top row heaters and 100 °C in the low row heaters. A new idea on the air draft chimney for harvesting freshwater from the discharged fluid by a total flow turbine in geothermal installations was verified. The influence of centre-to-centre row gap ratio on the thermal performance and the optimal ratio were determined. These outcomes can benefit the design and optimisation of the chimney in the future. This work is an extension of the work in [39] and has been undocumented in the literature so far.

In the following sections, three important issues will be discussed to better understand effects of boundary condition on heater surface and thermal radiation among the heaters between two rows on the thermal power and connective Nusselt number of the low row heaters. The optimal operating condition and geometrical parameter, limitations and further work will be addressed as well.

4.1. Effect of boundary condition

A uniform wall heat flux was prescribed as a boundary condition on the surface of each heater in the low and top rows in CFD simulations performed in the paper. Consequently, nonuniform wall temperature occurs in Fig. 16. Honestly, a uniform wall temperature can also be prescribed on the surface of each heater as a boundary condition. To identify the effect of two boundary conditions on heat transfer, the uniform wall heat flux was replaced with uniform wall temperature in the case Δy=8d, and the corresponding CFD simulations were relaunched, the predicted thermal power and convective Nusselt number of the low row heaters are illustrated in Fig. 19.

It is evident that the thermal power and convective Nusselt number

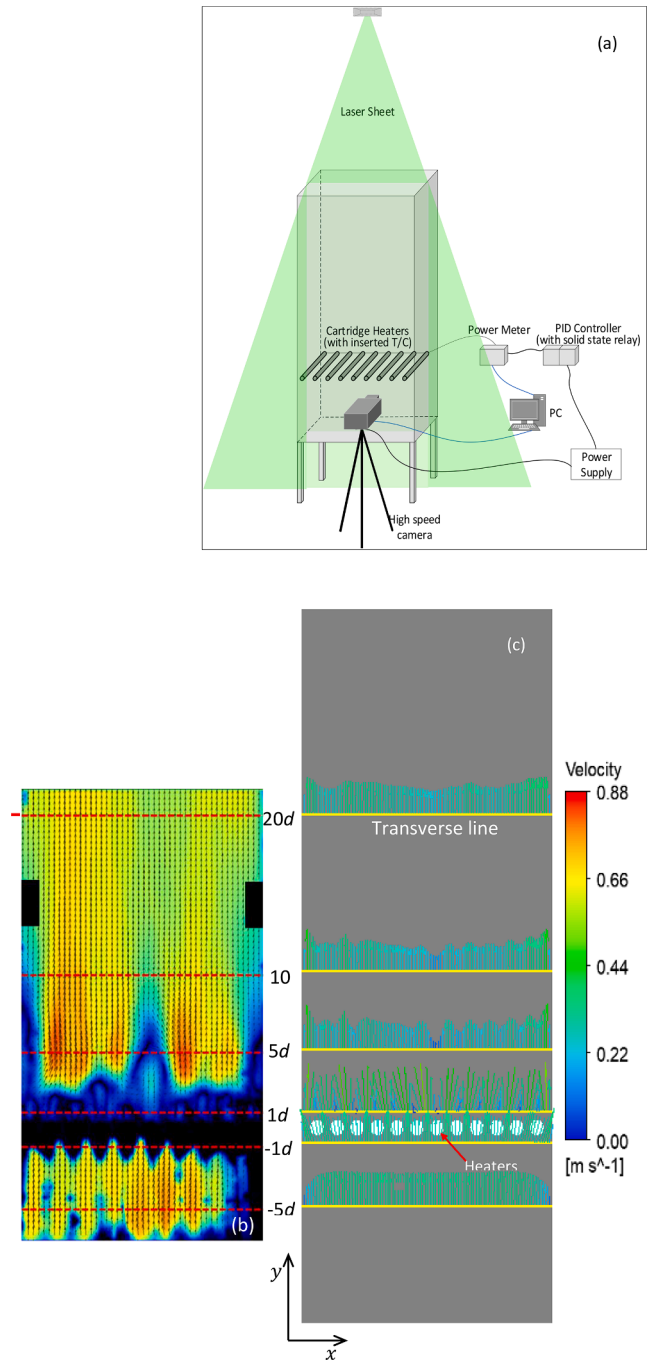

Fig. A1. Sketch of PIV experimental installation of the thermal chimney (a), velocity vector plot in the mid-span plane in the chimney measured by PIV at 160°C (b), and six transverse lines are indicated with velocity vectors predicted by the CFD simulation (c), the vertical velocity u_y is extracted from PIV measurements and compared with those in CFD simulations, d is the heater outer diameter.

based on wall temperature condition are smaller by (1.3–8.8) % and (1.5–10.3) %, respectively, resulting in an increased error compared with the experimental data. Especially, the thermal power and convective Nusselt number decline at the nominal temperature higher than 180 ℃. This matter of fact suggests that the prescribed wall heat flux as a boundary condition is more reasonable than the prescribed wall temperature as a boundary condition.

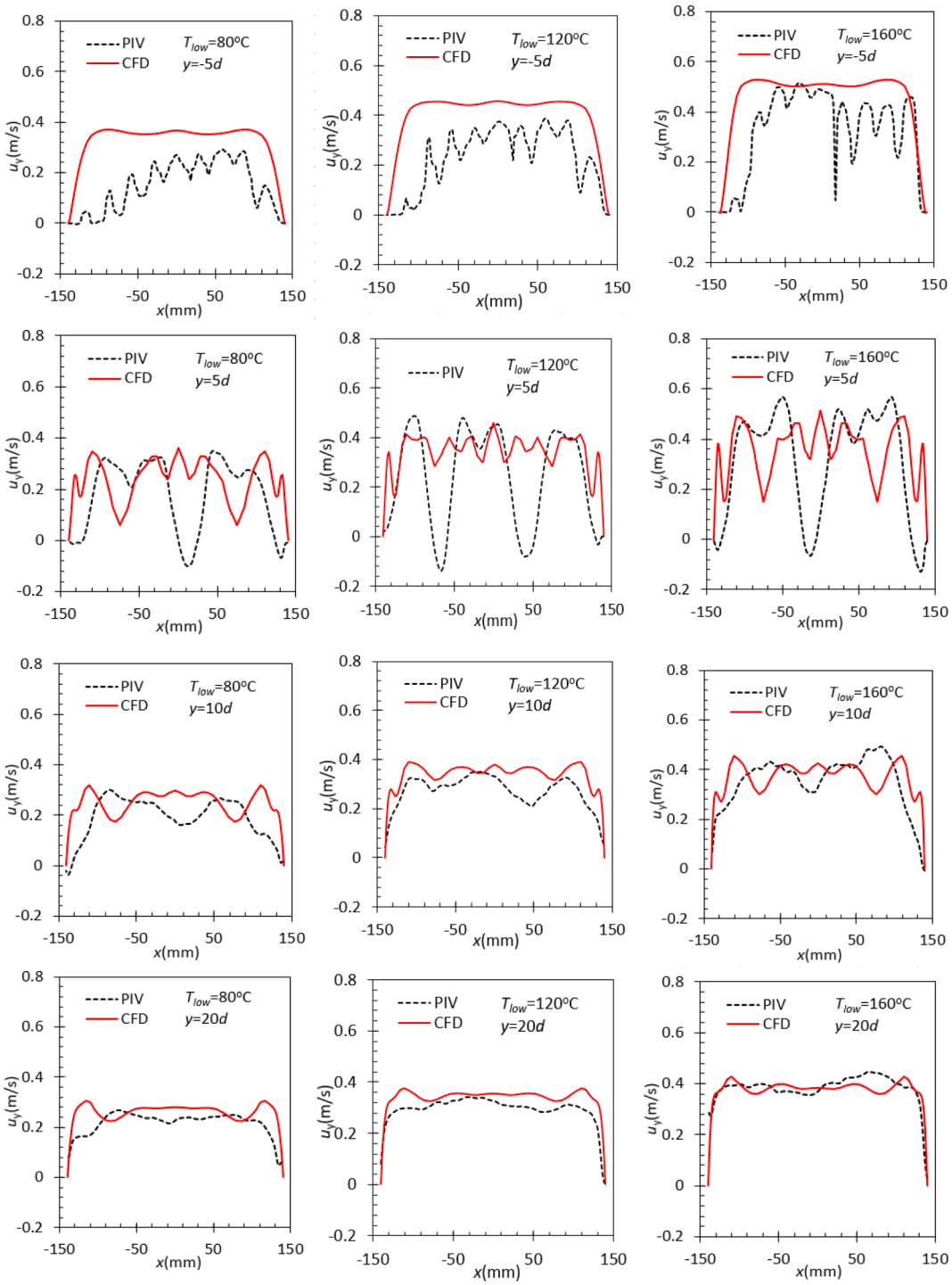

Fig. A2. Comparison of air vertical velocities between PIV and CFD at four transverse lines of y=± 5*d*, 10*d* and 20*d* in the mid-span plane as well as three heater temperaturesT_{low} = 80, 120, 160 ℃.

Table A1
Errors of the vertical velocity magnitude between PIV and CFD at three locations and three heater temperatures.

T(°C)	Mean u_y at 5*d* (m/s)			Mean u_y at 10*d* (m/s)			Mean u_y at 20*d* (m/s)		
	PIV	CFD	Error (%)	PIV	CFD	Error (%)	PIV	CFD	Error (%)
80	0.208	0.235	−13.0	0.204	0.248	−21.6	0.217	0.259	−14.6
120	0.258	0.341	−32.1	0.285	0.337	−18.2	0.306	0.335	−9.5
160	0.314	0.354	−12.7	0.354	0.370	−4.5	0.382	0.375	+1.8

Error=(PIV-CFD)/PIV × 100%.

4.2. Effect of thermal radiation between two row heaters

As shown in Fig. 7 and Fig. 9, the slope of experimental electrical power and convective Nusselt number curves becomes smaller with decreasing Δy. The slope of thermal power and convective Nusselt number curves predicted demonstrates that behaviour as well. This effect may be related to the thermal radiation of the top row heaters to the low row heaters. Unfortunately, there is no way to extract the information about the thermal radiation between two surfaces in ANSYS CFX at all. Therefore, an analytical solution of radiative heat transfer between two parallel cylinders with infinite length has to be employed to estimate the thermal radiation power of the top row heaters to the low row heaters in an approximate manner. Based on the analytical solution of radiative heat transfer between a pair of infinitely long parallel cylinders with the same diameter but different uniform surface temperatures presented in [56], the thermal radiation power $Q_{r\mathscr{i}\mathscr{j}}$ from the heater $\mathscr{j}$ in the top row to the heater $\mathscr{i}$ in the low row as illustrated in Fig. 3 is calculated by:

$$Q_{r\mathscr{i}\mathscr{j}} = \varepsilon\sigma A\frac{1}{\pi}\left(\sin^{-1}\frac{1}{\frac{\Delta_{\mathscr{i}\mathscr{j}}}{d}} + \sqrt{\left(\frac{\Delta_{\mathscr{i}\mathscr{j}}}{d}\right)^2 - 1} - \frac{\Delta_{\mathscr{i}\mathscr{j}}}{d}\right)\left(T_{top}^4 - T_{low}^4\right) \tag{13}$$

where $\Delta_{\mathscr{i}\mathscr{j}}$ is the centre-to-centre distance between the heater $\mathscr{i}$ and the heater $\mathscr{j}$, $\Delta_{\mathscr{i}\mathscr{j}} = \sqrt{[(\mathscr{i}-\mathscr{j})\Delta x]^2 + (\Delta y)^2}$. Then, the mean thermal radiation power from the top row heaters to the low row heaters is determined by:

$$Q_r = \frac{1}{N}\sum_{\mathscr{i}=1}^{N}\sum_{\mathscr{j}=1}^{N} Q_{r\mathscr{i}\mathscr{j}} \tag{14}$$

where Q_r is the mean thermal radiation power, N is the number of heaters in the top or low row, N=10. Based on Eqs. (13) and (14), a MATLAB code was compiled to calculate Q_r, and the corresponding results are presented in Fig. 20.

In the figure, positive mean thermal radiation power indicates that the low row heaters absorb thermal radiation power from the top row heaters, while negative thermal radiation power suggests the low row heaters issue thermal radiation power to the top row heaters. The sharpest rise curve of the mean thermal radiation power with increasing nominal temperature is seen at $\Delta y = 2d$ row gap, then the curve becomes flat after $\Delta y \geq 5d$. The mean thermal radiation power declines with increasing Δy at a fixed nominal temperature, especially at a temperature higher than 120 ℃. Overall, the mean thermal radiation power can play a role in heat transfer at Δy=2d-5d and T_{top} = 120–200 ℃. In this regard, the increased mean thermal radiation power from the top heaters to the low row heaters is responsible for the reduced slope of experimental electrical power and convective Nusselt number curves with increasing nominal temperature at $\Delta y = 2d$-5d.

According to Fig. 7 and Fig. 9, the predicted thermal power and convective Nusselt number are smaller than the corresponding experimental data, especially at $\Delta y = 8d$. To identify the reason for this effect, the emissivity value of heater surfaces was altered to $\varepsilon = 0.59$ from $\varepsilon = 0.27$, and CFD simulations were relaunched at Δy=8d, the thermal power and convective Nusselt number are shown in Fig. 21.

Clearly, a large emissivity value of the heater surfaces can raise the thermal power but can increase the convective Nusselt number a little only. Hence, the flow and convective heat transfer models adopted in the paper might be the reason for the small thermal power and convective Nusselt number predicted in CFD simulations in comparison with the experimental data. A further study is worth being conducted in the future.

4.3. Effect of computational domain

Initially, a complex fluid–solid domain as shown in Fig. 22 was specified. The chimney was included in the corresponding conjugate heat transfer simulations as a solid domain. The chimney walls become the interfaces between the air inside the chimney and the air outside the chimney. In that case, the thermal radiation between the heaters and the chimney walls cannot be set up due to the limitation in CFX-Pre. The material of the chimney is plastic with large thermal resistance; thus, the higher temperature is confined in the region near the heaters only, and the temperature as low as 20℃ in the rest region, see Fig. 22. Simulations with surface-to-surface radiation require over 5 million mesh cells, causing an over-loaded computational effort on our desktop. As a result, the chimney was removed, and the computational domain is simplified as Fig. 3. In this case, the thermal radiation between the heaters and the chimney walls can be set up properly. The wall temperature contour of the chimney predicted with the complex solid–fluid domain and a rough mesh (≈2.5 million cells) T_{top} = 140 ℃ is illustrated in Fig. 22. It is seen that the chimney wall is subject to a nonuniform temperature profile in the areas near the two row heaters on the chimney walls.

The thermal powers and convective Nusselt numbers predicted with the complex solid–fluid domain are plotted as a function of top row heater temperature in Fig. 23. The thermal power and convective Nusselt number predicted with the complex domain are slightly different from those with the simple domain in numerical values. However, the convective Nusselt number Nu_c is still the highest at Δy=5d, as shown in Fig. 24. Thus, the geometrical configuration at $\Delta y = 5d$ remains optimal in the case of the complex solid–fluid domain.

4.4. Optimal operating and geometrical conditions

In Fig. 6, the chimney energy gain coefficient η_{th} is the best at $\Delta y = 5d$ and $T_{low} \geq 140$ ℃ compared with the coefficients at Δy=2d, 8d. Based on Fig. 9 and Fig. 10, the Nusselt number Nu_c is the highest at $\Delta y = 5d$ in comparison with those at Δy=2d, 8d. The optimal operating condition should be at a nominal temperature of $T_{low} \geq 140$ ℃ in terms of energy saving. The optimal geometrical condition should be $\Delta y = 5d$ for this chimney and $\Delta x = 1.75d$ from convective heat transfer point of view. This value is in the optimal range $\Delta y = 4.5d$-6d proposed in [38] based on 2D CFD simulations.

4.5. Limitation and future work

The experimental electrical power of a single heater in the low row was compared with the thermal power calculated by wall heat flux prescribed in a CFD simulation as shown in Fig. 7. Note that the thermal power generated by a heater should be smaller by heater efficiency than the electrical power consumed by the heater. Since the information on the heater efficiency cannot be found in the manufacturer's datasheet and in the literature, the electrical power has to be adapted here. Hopefully, this drawback will be removed in the future.

In CFD simulations, proper uniform wall heat fluxes were applied onto the top and low row heaters to match the experimental nominal temperatures of the heaters in two rows. As a result, the predicted temperature on the surface of each heater is nonuniform. Even though this phenomenon is similar to that revealed experimentally in [39], experimental evidence is unavailable to support the phenomenon based on the chimney with two row heaters presently. The temperature distribution on two row heaters in the chimney needs to be conducted in the future.

It should be noted that heat transfer experiments and CFD simulations were started from a temperature as low as 60 ℃ to obtain a wide range of Reynolds numbers. This is purely in terms of the perspective of convective heat transfer. However, based on Fig. 2, just the results of convective heat transfer for the top row heaters to operate at or above the temperature 100 ℃ can be meaningful to the design of the thermal chimney for geothermal applications.

As shown in Fig. 12 and Fig. 13, there are thick boundary layers on the walls of the chimney. To improve the thermal performance of the chimney these boundary layers should be kept as thin as possible. In this

context, the shape of the cross-section and profile of the chimney should be altered and optimised by using analysis, experiment and CFD simulation in the future. The typical existing studies have provided us with sound starting points for optimising the shape of the cross-section and profile of the chimney with analytical methods [57] and CFD simulations [58,59].

Our current experimental facility cannot simulate the phase change of steam. In the future, the secondary heat exchanger should be replaced with a coil heat exchanger or another type of heat exchanger. A stream of steam is introduced into the exchanger to check the cooling effect and steam condensation by the draft air in the chimney. The heat exchanger should install additional elements to enhance its heat transfer. The other further studies are listed in phase 3 as shown in Fig. 1.

5. Conclusion

The convective heat transfer of air in a designed thermal chimney with two row electrical heaters was studied by using experiment and CFD software ANSYS 2019R CFX when the top row heaters were operated at 60, 80, 100, 120, 140, 160, 180, 200 ℃ nominal temperatures and the low row heaters at 100 ℃ nominal temperature under 20 ℃ ambient temperature condition. CFD simulations are based on 3D, steady RANS equations with the Boussinesq buoyancy model, $k-\omega$ two-equation turbulence model, and energy equation of air. The thermal radiation between heater surfaces and chimney walls is taken into account. The overall thermal performance of the chimney, heat transfer characteristics, temperature and flow fields in the chimney were detailed. Effects of both boundary condition of heater surface and thermal radiation between two row heaters on heat transfer were argued. Based on the results shown in Section 3 and 4, a couple of concluding points are summarised:

(1). The top row heaters in the chimney can induce an upwards air flow and cool the low row heaters, thus our design concept on the thermal chimney for geothermal applications to produce freshwater was verified. Generally, the thermal characteristics of the chimney with two row heaters, including temperature rise, air mass flow, energy gain coefficient, heater and chimney Reynolds numbers, are better than the chimney with single row heaters, especially at$\Delta y = 5d$. The convective Nusselt number of the low row heaters is also larger than the number of the single row heaters. The predicted thermal power and convective Nusselt number agree well with the experimental data.

(2). The optimal operating nominal temperature of top row heaters should be $\geq$ 140 ℃, and the optimal centre-to-centre row gap Δy is in the range of (5–6)d, andΔy = - 5d is a quite reasonable choice. In that case, the convective Nusselt number of the low row heaters is enhanced by (11.6–29.8) %, depending on their nominal temperature or Reynolds number compared with the case with single row heaters.

(3). Multiple jets in the gaps among the heaters in each row exist when the air passing through each row of the heaters in the chimney. Whether the jets mix each other after leaving the low row or top row depends on Δy. As the air passes through two rows of heaters, its velocity reaches the maximum at the throat in the gaps among heaters in a row. After the air leaving from the top row heaters, the air velocity reduces considreably and becomes uniform gradually. The maximum of the velocity rises with increasing heater nominal temperature. Two peaks in air temperature occur at the leading and trailing edges of the heaters when the air crosses two heater rows. There is a jump in air temperature after crossing each row of heaters, and the temperature declines until the exit of the chimney, and the jumps are enlarged with incresing heater nominal temperature.

(4). There are boundary layers on the chimney walls, and the thinnest boundary layer or the largest size core flow is observed at$\Delta y = 5d$. The boundary layer thickness apparently varies slightly with increasing nominal temperature of the top row heaters.

(5). A prescribed wall heat flux as a boundary condition on the heater surface leads to uneven temperature distribution on heat surfaces and is more reasonable than a prescribed wall temperature as a boundary condition. The mean thermal radiation power between two rows of heaters can play a part in heat transfer at Δy=2d-5d andT_{top} = 120–200 ℃. The increased mean thermal radiation power from the top heaters to the low row heaters is attributed to the reduced slope of experimental electrical power and convective Nusselt number curves with increasing nominal temperature atΔy = 2d-5d.

The further research issues may be focused on the shape optimisation of cross-section and profile of the chimney, investigation into coil heat exchanger or another type of heat exchanger as the secondary heat exchanger to check the cooling and phase change effects by the draft air in the chimney when steam flowing in the exchanger, as well as study on heat transfer enhancement of the exchanger with additional devices.

Declaration of Competing Interest

The authors declare that they have no known competing financial interests or personal relationships that could have appeared to influence the work reported in this paper.

Data availability

Data will be made available on request.

Acknowledgement

Zhibin Yu and Wenguang Li would like to acknowledge the financial support provided by EPSRC (EP/T022701/1, EP/V042033/1, EP/P028829/1, EP/N020472/1, EP/N005228/1, EP/V030515/1) in the UK.

Appendix A. . Validation of flow field with PIV measurements

PIV measurements were conducted in our group to obtain the velocity profile in the mid-span plane of the chimney with heaters in a single row at three heater temperatures: 80, 120, 160 ℃. The PIV experimental installation is sketched in Fig. A1. The chimney is positioned in the middle of the isolated test section of a large wind tunnel. The space in the test section is so large that air can develop under and above the chimney. Flow field in the chimney was illuminated by a Nd: YAG laser with 100 mJ pulses of 8 ns duration at a maximum repetition rate of 200 Hz, and the field view is captured by a 4-megapixel Phantom v341 digital high-speed camera. The PIV laser light sheet was shot from the top and covered the mid-span plane. The time delay between image pairs was 0.5–2.2 ms, depending on heater temperature and velocity magnitudes in the chimney to resolve the flow field properly. Image pairs of 600 at a rate of 3 per second were taken for each experimental configuration. The raw PIV images were processed by using LaVison Davis 8 and MATLAB. The relationship of coordinate system between the chimney and the camera was calibrated before recording images. An example of velocity mapped by PIV at the heater temperature of 160 °C is shown in Fig. A1. The correlation between two images fails in the dark

regions due to significant noise in them, and the velocities in the region between two horizontal lines at $y=\pm 1d$ are missing, thus these velocities are ignored and not compared with CFD simulation.

The vertical velocities of the air were extracted from PIV and CFD databases at four horizontal lines of $y=\pm 5d$, $10d$ and $20d$ indicated in Fig. A1, and compared in Fig. A2. At $y=-5d$ horizontal line (upstream near the heaters), the PIV leaser was shadowed by the heaters, the information on air velocity is incomplete and the velocity exhibits distorted profiles, thus does not have any similarity to the velocity profiles predicted by CFD. The distorted profiles were due to residual crosswind in the test section.

At $y=5d$ horizontal line (downstream near the heaters), the velocity profile in PIV becomes almost symmetrical and has a few negative peaks at three temperatures. In the velocity profiles predicted by CFD, negative velocities do not exist at all. At $y=10d$ and $20d$ horizontal lines (downstream far the heaters), the velocity profiles predicted are similar to the PIV measurements.

The errors of the velocity between PIV and CFD at three temperatures$T_{low}=80$, 120, 160 ℃ are listed in Table A1. Basically, the errors are in a range of (-30- + 2)%, depending on the temperature.

References

[1] D.J. Ryley, Geotherml energy-problems in heat and fluid flow, International Journal of Heat and Fluid Flow 3 (3) (1982) 115–123.

[2] IRENA, " Geothermal Power: Technology Brief," International Renewable Energy Agency, Abu Dhabi, 2017.

[3] K. Akagawa, T. Fujii, S. Takagi, M. Takeda, K. Tsuji, Performance of a Hero's turbine using two-phase mixture as a working fluid, Transcations of Japan Society of Mechanical Engineers-Series B 50 (452) (1983) 1159–1165.

[4] K. Akagawa, T. Fujii, J. Ohta, S. Takagi, Cycle performance of total flow turbine system (1st Report, utlization of saturated hot water), Transcations of Japan Society of Mechanical Engineers-Series B 52 (480) (1986) 3052–3058.

[5] K. Akagawa, T. Fujii, J. Ohta, S. Takagi, Cycle performance of total flow turbine system (2nd Report, utlization of wet steam), Transcations of Japan Society of Mechanical Engineers-Series B 54 (502) (1988) 1509–1515.

[6] L. Hu, Z. Wang, W. Fan, F. Pang and C. Lu, "An organic total flow system for geothermal energy and waste heat conversion," in *Proceedings of the 24th Intersociety Energy Conversion Engineering Conference, , pp. 2161-2165 vol.5, doi: 10.1109/IECEC.1989.74773.*, Washington D C, USA, 1989.

[7] M.A. Iqbal, M. Ahmadi, F. Melhem, S. Rana, A. Akbarzadeh, A. Date, Power generation from low grade heat using trilateral flash cycle, Energy Procedia 110 (2017) 492–497.

[8] M.A. Iqbal, S. Rana, M. Ahmadi, A. Date, A. Akbarzadeh, Trilateral flash cycle (TFC): A promising thermodynamic cycle for low grade heat to power generation, Energy Procedia 160 (2019) 208–214.

[9] V. Zare, A comparative exergoeconomic analysis of different ORC configurations for binary geothermal power plants, Energy Conversion and Management 105 (2015) 127–138.

[10] N. Shokati, F. Ranjbar, M. Yari, Comparative and parametric study of double flash and single flash/ORC combined cycles based on exergoeconomic criteria, Applied Thermal Engineering 91 (2015) 479–495.

[11] D. Meng, Q. Liu, Z. Ji, Effects of two-phase expander on the thermoeconomics of organic double-flash cycles for geothermal power generation, Energy 239 (2022) 122346.

[12] M. El Haj Assad, Y. Aryanfar, A. Javaherian, A. Khosravi, K. Aghaei, S. Hosseinzadeh, J. Pabon, S.M.S. Mahmoudi, Energy, exergy, economic and exergoenvironmental analyses of transcritical CO_2 cycle powered by single flash geothermal power plant, International Journal of Low-Carbon Technologies 16 (2021) 1504–1518.

[13] N. Shokati, F. Ranjbar, M. Yari, Exergoeconomic analysis and optimization of basic, dual-pressure and dual-fluid ORCs and Kalina geothermal power plants: A comparative study, Renew Energy 83 (2015) 527–542.

[14] J. Wang, J. Wang, Y. Dai, P. Zhao, Thermodynamic analysis and optimization of a flash-binary geothermal power generation system, Geothermics 55 (2015) 69–77.

[15] Z. Wang, H. Zhou, M. Hao, J. Wang, M. Geng, Thermodynamic analysis and comparative investigation of a novel total flow and Kalina cycle coupled system for fluctuating geothermal energy utilization, Energy 260 (2022) 125066.

[16] J. Bundschuh, N. Ghaffour, H. Mahmoudi, M. Goosen, S. Mushtaq, J. Hoinkis, Low-cost low-enthalpy geothermal heat for freshwater production: Innovative applications using thermal desalination processes, Renewable and Sustainable Energy Reviews 43 (2015) 196–206.

[17] V.G. Gude, Geothermal source potential for water desalination – Current status and future perspective, Renewable and Sustainable Energy Reviews 57 (2016) 1038–1065.

[18] T.M. Missimer, K.C. Ng, K. Thuw, M.W. Shahzad, Geothermal electricity generation and desalination: An integrated process design to conserve latent heat with operational improvements, Desalination and Water Treatment 57 (2016) 23110–23118.

[19] A. Farsi, M.A. Rosen, Assessment of a geothermal combined system with an organic Rankine cycle and multi-effect distillation desalination, Earth Systems and Environment 6 (2022) 15–27.

[20] S. Loutatidou, H.A. Arafat, Techno-economic analysis of MED and RO desalination powered by low-enthalpy geothermal energy, Desalination 365 (2015) 277–292.

[21] F. Calise, M.D. d'Accadia, A. Macaluso, L. Vanoli, A. Piacentino, A novel solar-geothermal trigeneration system integrating water desalination: Design, dynamic simulation and economic assessment, Energy 115 (2016) 1533–1547.

[22] F. Calise, A. Macaluso, A. Piacentino, L. Vanoli, A novel hybrid polygeneration system supplying energy and desalinated water by renewable sources in Pantelleria Island, Energy 137 (2017) 1086–1106.

[23] A. Christ, B. Rahimi, K. Regenauer-Lieb, H.T. Chua, Techno-economic analysis of geothermal desalination using hot sedimentary aquifers: A pre-feasibility study for Western Australia, Desalination 404 (2017) 167–181.

[24] H. Mahmoudi, N. Spahis, M.F. Goosen, N. Ghaffour, N. Drouiche, A. Ouagued, Application of geothermal energy for heating and fresh water production in a brackish water greenhouse desalination unit: A case study from Algeria, Renewable and Sustainable Energy Reviews 14 (2010) 512–517.

[25] M. Capocelli, E. Moliterni, V. Piemonte, M. De Falco, Reuse of waste geothermal brine: Process, thermodynamic and economic analysis, Water 12 (2020) 316.

[26] M. Prajapati, M. Shah, B. Soni, A review of geothermal integrated desalination: A sustainable solution to overcome potential freshwater shortages, Journal of Cleaner Production 326 (2021) 129412.

[27] Y. Zhao, A. Akbarzadeh, J. Andrews, Simultaneous desalination and power generation using solar energy, Renewable Energy 34 (2009) 401–408.

[28] F. Bai, A. Akbarzadeh and R. Singh, "Combined fresh water production and power generation from geothermal reservoirs," in *Proceedings World Geothermal Congress 2010* , Bali, Indonesia, 2010.

[29] A. Date, F. Alam, A. Khaghani, A. Akbarzadeh, Investigate the potential of using trilateral flash cycle for combined desalination and power generation integrated with salinity gradient solar ponds, Procedia Engineering 49 (2012) 42–49.

[30] A. Khaghani, "Dual thermal system for power and fresh water production, PhD Thesis," RMIT University, Melbourne, Australia, 2013.

[31] A. Date, A. Khaghani, J. Andrews, A. Akbarzadeh, Performance of a rotating two-phase turbine for combined power generation and desalination, Applied Thermal Engineering 76 (2015) 9–17.

[32] G. Yu, Y. Z, Investigation of geothermal sourced combined power and freshwater generation systems, Energy Procedia 158 (2019) 5946–5953.

[33] G. Yu, Z. Yu, Combined power and freshwater generation driven by liquid-dominated geothermal sources, Energies 12 (8) (2019).

[34] G. Yu, Z. Yu, Research on a coupled total-flow and single-flash (TF-SF) system for power and freshwater generation from geothermal source, Applied Sciences 10 (8) (2020).

[35] S. Rane, L. He, CFD analysis of flashing flow in two-phase geothermal turbine design, Journal of Computational Design and Engineering 7 (2) (2020) 238–250.

[36] H. Li, S. Rane, Z. Yu, Investigation of the performance and flow characteristics of two-phase reaction turbines in total flow geothermal systems, Renewable Energy 175 (2021) 345–372.

[37] H. Ma, L. He and S. Rane, "Heat transfer-fluid flow interaction in natural convection around heated cylinder and its thermal chimney effect," in *Proceedings of the International Conference on Innovative Applied Energy, 14-15 March*, Oxford, UK, 2019.

[38] H. Ma, L. He, G. Yu, Z. Yu, Natural convection heat transfer and fluid flow in a thermal chimney with multiple horizontally-aligned cylinders, International Journal of Heat and Mass Transfer 183 (2022) 122239.

[39] W. Li, G. Yu, D. Zagaglia, R. Green, Z. Yu, CFD modelling of a thermal chimney for air-cooled condenser, Geothermics 88 (2020) 101908.

[40] G. Yu, D. Zagaglia, R. Green, Z. Yu, Particle Image Velocimetry (PIV) experiment of the buoyant flow field of a thermal chimney model designed for geothermal power plants, International Journal of Green Energy 17 (15) (2020) 951–960.

[41] Ansys, CFX-solver theory guide, release 14.0, southpointe, ANSYS Inc, Canonsburg, USA, 2011.

[42] D.D. Gray, A. Giorcini, The validity of the boussinesq approximation for liquids and gases, International Journal of Heat and Mass Transfer 19 (5) (1976) 545–551.

[43] F.J. McQuillan, J.R. Culham, M.M. Yovanovich, Properties of dry air at one atmosphere, University of Waterloo, Waterloo, Canada, Microelectronics Heat Transfer Lab, 1984.

[44] Z. Wang, M. Yang, L. Li, Y. Zhang, Combined heat transfer by natural convection – conduction and surface radiation in an open cavity under constant heat flux heating, Numerical Heat Transfer, Part A: Applications 60 (4) (2011) 289–304.

[45] A.K.A. Shati, S.G. Blakey, S.B.M. Beck, A dimensionless solution to radiation and turbulent natural convection in square and rectangular enclosures, Journal of Engineering Science and Technology 7 (2) (2012) 257–279.

[46] S. Trabelsi, W. Lakhal, E. Sediki, M. Moussa, Nusselt number evaluation for combined radiative and convective heat transfer in flow of gaseous products from combustion, Thermal Science 17 (4) (2013) 1093–1106.

[47] S. Saravanan, C. Sivaraj, Coupled thermal radiation and natural convection heat transfer in a cavity with a heated plate inside, International Journal of Heat and Fluid Flow 40 (2013) 54–64.
[48] S. Hamimid, M. Guellal, Numerical study of combined natural convection-surface radiation in a square cavity, Fluid Dynamics & Materials Processing 10 (3) (2014) 377–393.
[49] M.F. Nia, S.A.G. Nassab, Conjugate heat transfer study of combined radiation and forced convection turbulent separated flow, International Journal of Nonlinear Sciences and Numerical Simulation 18 (1) (2017) 29–39.
[50] Z. Sert, M. Tekkalmaz, C. Timuralp, Combined natural convection and thermal radiation in an inclined cubical cavity with a rectangular pins attached to its active wall, Periodicals of Engineering and Natural Sciences 5 (3) (2017) 347–354.
[51] R. Hilpert, Heat emission from heated wires and pipes in the air stream, Engineering Research 4 (5) (1933) 215–224.
[52] R.M. Fand, K.K. Keswani, A continuous correlation equation for heat transfer from cylinders to air in crossflow for Reynolds numbers from 10^{-2} to 2×10^{5}, International Journal of Heat and Mass Transfer 15 (3) (1972) 559–565.
[53] A. Zukauskas, Heat transfer from tubes in crossflow, Advances in Heat Transfer 18 (1972) 93–160.
[54] S. Whitaker, Forced convection heat transfer correlations for flow in pipes, past flat plates, single cylinders, single spheres, and for flow in packed beds and tube bundles, AIChE Journal 189 (12) (1972) 361–371.
[55] S.W. Churchill, M. Bernstein, A correlating equation for forced convection from gases and liquids to a circular cylinder in cross-flow, ASME Journal of Heat Transfer 99 (2) (1977) 300–306.
[56] M.F. Modest, Radiative Heat Transfer, 3rd edition, Academic Press, Oxford, 2013.
[57] T.S. Fisher, K.E. Torrance, K.K. Sikka, Analysis and optimization of a natural draft heat sink system, IEEE Transactions on Components, Packaging, and Manufacturing Technology-Part A 20 (2) (1997) 111–119.
[58] S. Hu, D.Y.C. Leung, J.C.Y. Chan, Impact of the geometry of divergent chimneys on the power output of a solar chimney power plant, Energy 120 (2017) 1–11.
[59] H. Nasraoui, Z. Driss, H. Kchaou, Effect of the chimney design on the thermal characteristics in solar chimney power plant, Journal of Thermal Analysis and Calorimetry 140 (2020) 2721–2732.